Agricultural and Forest Meteorology 327 (2022) 109197

Contents lists available at ScienceDirect

Agricultural and Forest Meteorology

journal homepage: www.elsevier.com/locate/agrformet

Impact of radiation variations on temporal upscaling of instantaneous Solar-Induced Chlorophyll Fluorescence

Rui Cheng [a,b,*], Philipp Köhler [a,c], Christian Frankenberg [a]

[a] Division of Geological and Planetary Sciences, California Institute of Technology, Pasadena, CA, 91125, USA
[b] Department of Civil and Environmental Engineering, Massachusetts Institute of Technology, Cambridge, MA, 02139, USA
[c] EUMETSAT, Darmstadt, D-64295, Germany

ARTICLE INFO

Keywords:
Solar-Induced Chlorophyll Fluorescence
Length-of-day correction factor
Topography
Clear sky bias
Direct light
Diffuse light

ABSTRACT

Solar-Induced Chlorophyll Fluorescence (SIF) has been increasingly used as a novel proxy for vegetation productivity. Several space-borne instruments can retrieve SIF at varying overpass time, which complicates the interpretation as SIF is driven by absorbed Photosynthetically Active Radiation (PAR) at the acquisition time. To facilitate comparisons across sensors, satellite-based SIF is upscaled to daily averages with a length-of-day correction factor (DC). In conventional DC calculations, the light intensity over a day is approximated geometrically by the cosine of the Solar Zenith Angle (SZA), neglecting changes in atmospheric extinction and topographic effects. Here, we use reanalysis PAR data for DC calculations to evaluate the impact of atmospheric extinction and diffuse radiation individually. We find that the simple SZA approach is a reliable approximation for flat surfaces, where the overall atmospheric impact on DC is less than 10% as large individual effects on direct and diffuse PAR partially compensate each other. At longer time-scales, a sampling (clear sky) bias might exist due to cloud-filtering of satellite data. We find that in the Amazon the true monthly mean PAR can be 25% lower than the one for cloud-filtered days, potentially inducing seasonal SIF biases on the same order. An additional factor impacting PAR during a day is topography. For complex terrain, direct light in the DC expression requires a correction for surface slopes. For example in the San Gabriel Mountains, California, USA, the modified DC is changed by as much as 500% for strongly tilted surfaces. This modification is especially important for satellite instruments with fine spatial resolutions, where surface slopes are not averaged out and can have a substantial impact on reflectance and SIF. Overall, our refined DC-corrections and averaging strategy can help satellite SIF interpretation as well as intercomparisons over a wide range of spatio-temporal scales and overpass times.

1. Introduction

Photosynthesis is the dominant driver of land-atmosphere carbon exchange with poorly known climate feedbacks (Richardson et al., 2013). Solar-Induced Chlorophyll Fluorescence (SIF) has become a popular proxy for photosynthesis because it is linked to the electron transport rate in the light reactions of photosynthesis (Porcar-Castell et al., 2014). Many studies have used SIF to study photosynthesis on the global scale (Mohammed et al., 2019), including the estimation of gross primary production, canopy water deficit, and crop yield (Gentine and Alemohammad, 2018; Zuromski et al., 2018; He et al., 2020). Global scale studies in particular benefit from space-borne observations of SIF, which are relatively coarse in the spatial domain but a valuable tool for monitoring photosynthesis without requiring sub-pixel homogeneity. As more satellites measure SIF, comparisons across sensors are challenging due to varying times of measurement (t_m).

SIF inferred from satellite measurements (SIF_{t_m}) represents the radiance emitted by chlorophyll that primarily depends on the amount of Absorbed Photosynthetically Active Radiation (APAR) at t_m (Magney et al., 2020; Mohammed et al., 2019; Joiner et al., 2020), which is a product of Photosynthetically Active Radiation (PAR) reaching the canopy at t_m and the fraction of PAR absorbed by the canopy (fPAR). Because PAR varies across ground tracks (Köhler et al., 2018; Joiner et al., 2020) and with satellite orbital parameters, while the diurnal cycle of fPAR is negligible compared to the diurnal cycle of PAR (Lin et al., 2019), SIF_{t_m} is an instantaneous value associated with PAR at t_m. In order to compare SIF across different satellites with various t_m and against daily mean gross primary production (Zhang et al., 2018b,a), studies (Hu et al., 2018; Köhler et al., 2018; Zhang et al., 2018b; Frankenberg et al., 2011) have to scale SIF_{t_m} to a daily-average SIF

* Corresponding author at: Division of Geological and Planetary Sciences, California Institute of Technology, Pasadena, CA, 91125, USA.
E-mail address: rui.cheng@mit.edu (R. Cheng).

https://doi.org/10.1016/j.agrformet.2022.109197
Received 17 May 2022; Received in revised form 24 September 2022; Accepted 3 October 2022
Available online 2 November 2022

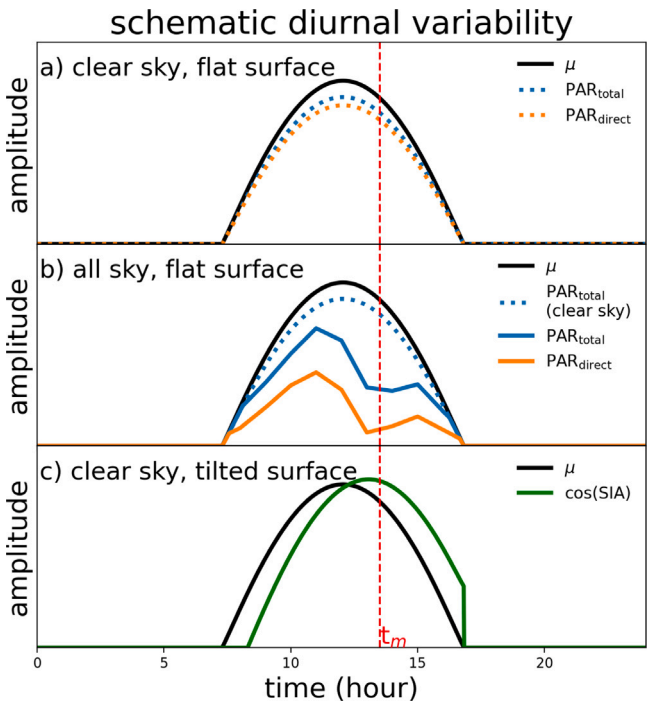

Fig. 1. Schematic diurnal cycles of μ, direct PAR (PAR_{direct}) and total PAR (PAR_{total}) under (a) clear-sky and (b) all sky conditions assuming the surface is flat, and (c) the cosine of Solar Incidence Angle (cos(SIA)) under clear-sky condition.

(SIF_{dc}) using a length-of-day correction factor (DC), which is calculated based on the diurnal cycle of PAR under the assumption that SIF scales linearly with PAR:

$$SIF_{dc} = SIF_{t_m} \times DC, \tag{1a}$$

$$DC = \frac{1}{PAR_{t_m}} \int_{t_m\text{-}12h}^{t_m+12h} PAR_t \, dt. \tag{1b}$$

Conventionally, the diurnal cycle of PAR in the calculation of DC (Eq. (1)b) is approximated geometrically by the cosine of Solar Zenith Angle (SZA), denoted as μ (Frankenberg et al., 2011; Köhler et al., 2018) (Fig. 1a). Thus, the derivation of the DC can be simplified to

$$DC_{SZA} = \frac{1}{\mu_{t_m}} \int_{t_m\text{-}12h}^{t_m+12h} \mu_t \, \mathcal{H}(\mu_t) \, dt, \tag{2}$$

where $\mathcal{H}$ is the Heaviside step function, i.e. zero for SZAs greater than 90° (nighttime).

This straightforward approach generates SIF_{dc} via DC_{SZA} without the need to know true PAR as μ_t can simply be computed using ephemeris calculators, which provide the solar geometry at a given location and time based on orbital parameters of the Earth in the solar system. The approximation is thus a simple yet possibly inaccurate proxy for PAR at the top of canopy, as the approach neglects atmospheric effects (Fig. 1b), e.g. changing cloud, as well as topography (Frankenberg et al., 2011)(Fig. 1c). As there is no detailed quantitative evaluation of the impact of atmospheric absorption and scattering as well as topography on the DC calculation, the potential errors in SIF averages are still hard to assess.

To characterize potential errors in conventional daily-average SIF calculations as well as in temporal (e.g. monthly) averages, we have to consider the following effects, illustrated using simple examples: (I) Diurnal atmospheric effects: diurnal cycles in atmospheric conditions (e.g. convective systems building up during a day) can cause biases when using a simple geometric approach and these will depend on the time of measurement; (II) Day-to-day atmospheric effects: cloud filtering of satellite data can cause a clear-sky bias in longer-term SIF averages, as the measurements passing the quality filters are more likely obtained during cloud free days; (III) Topography effects: topography can create highly asymmetric diurnal PAR cycles, as we have to consider the geometry of a tilted surface with respect to the sun.

Our study aims to quantify these impacts individually so that SIF measurements across sensors and temporal–spatial scales can be better compared and interpreted. In Section 2, we develop correction models (summarized in Table 1) for DC. Using global PAR datasets, solar angle information, detailed topography, and actual SIF soundings, as outlined in Section 3, we evaluate the DC calculations in Section 4. At the global scale, we highlight areas where temporal upscaling SIF is prone to biases by atmospheric effects and use regional examples to quantify the individual bias in areas with strong seasonal variations in cloud cover (e.g. the Amazon) and complex terrain (e.g. the San Gabriel Mountains).

2. Methods

2.1. Atmospheric effects

2.1.1. Upscaling SIF_{t_m} to SIF_{dc}

Downwelling PAR at the surface can be divided into two components: direct PAR (PAR_{direct}) and diffuse PAR ($PAR_{diffuse}$). PAR_{direct} is the transmitted part of the incoming collimated solar beam reaching the surface after being diminished by atmospheric extinction by trace gases, aerosols and clouds along the light path. Despite its reduced amplitude, PAR_{direct} preserves the direction of the incoming PAR, which is represented by the SZA. Because PAR at the top of atmosphere is directly proportional to μ, the difference between the diurnal cycles of PAR_{direct} and μ results from atmospheric extinction along the light path. Hence, we can evaluate this impact on SIF_{dc} by comparing DC_{SZA} with DC_{direct}, which is calculated with actual PAR_{direct}:

$$DC_{direct} = \frac{1}{PAR_{direct,t_m}} \times \int_{t_m\text{-}12h}^{t_m+12h} PAR_{direct,t} \, dt. \tag{3}$$

$PAR_{diffuse}$ is constituted by scattered PAR that ultimately reaches the surface. $PAR_{diffuse}$ can also be the major energy source for photosynthesis when PAR_{direct} is strongly reduced through atmospheric scattering, e.g. at high latitudes or in areas with frequent cloud cover. Thus, in order to accurately account for changes in total PAR, a comprehensive DC correction factor needs both PAR_{direct} and $PAR_{diffuse}$:

$$DC_{total} = \frac{1}{\left(PAR_{direct,t_m} + PAR_{diffuse,t_m}\right)} \times \int_{t_m\text{-}12h}^{t_m+12h} \left(PAR_{direct,t} + PAR_{diffuse,t}\right) dt. \tag{4}$$

Thus, the difference between DC_{total} and DC_{direct} is due to the impact of diffuse light. It is worth noting that plants can use diffuse light more efficiently than direct light (Gu et al., 2019, 1999; Lu et al., 2020), as it is distributed more evenly across the top of the canopy. Here, we neglect this and focus on variations in total PAR, i.e. assume that both PAR_{direct} and $PAR_{diffuse}$ have a similar impact on SIF.

To isolate the impact of clouds, we can make use of the fact that meteorological reanalysis data are provided for both all-sky conditions (including all atmospheric effects as modeled) as well as clear sky conditions (providing radiation fields as if no clouds had been present). This allows us to separate the atmospheric effects on SIF_{dc} for cloud free conditions in Section 4.1.1 and all-sky (i.e. most realistic) conditions in Section 4.1.2. With the help of these globally modeled PAR datasets, we can highlight regions where atmospheric effects are important to consider in SIF_{dc} with and without clouds.

2.1.2. Upscaling SIF_{dc} to monthly mean SIF ($\overline{SIF}$)

In addition to scaling biases from the instantaneous SIF signal to a diurnal average, sampling biases can occur when aggregating individual daily averages in time, for instance to monthly scales. Unlike vegetation indices, SIF is not only representing a slowly varying canopy structure but is also driven by highly variable incoming PAR, which is strongly impacted by clouds. As cloudiness is also as a selection criteria for satellite data quality filtering, this can cause potential sampling biases.

Often, monthly-mean SIF ($\overline{\mathrm{SIF}}$) is calculated as the cloud-filtered arithmetic mean of $\mathrm{SIF_{dc}}$ within the temporal averaging window (Sun et al., 2018; Badgley et al., 2017). However, cloud filters preferentially keep the soundings that are taken under low cloud cover (i.e. situations with higher PAR), which potentially result in a clear sky bias (Zhang et al., 2020; Sun et al., 2018; Badgley et al., 2017) that can vary seasonally.

Thus, seasonal variations in the number of cloud-filtered soundings relative to total number of soundings can be used as a metric for the potential clear sky bias. In Section 4.1.3.1, we use statistics from the TROPOspheric Monitoring Instrument (TROPOMI) as well as reanalysis data to investigate when and where globally the clear sky bias is likely to occur.

To quantify the actual clear sky bias, Hu et al. (2021) suggested weighing $\mathrm{SIF_{dc}}$ by daily mean PAR. Here, we upscale $\mathrm{SIF_{dc}}$ to $\overline{\mathrm{SIF}}$ using the daily mean all-sky PAR ($\overline{\mathrm{PAR}}_{\mathrm{day}}$) just from measurement days and from all days in a month. Then, the actual clear sky bias is the difference between PAR-weighted $\overline{\mathrm{SIF}}$ and the arithmetic $\overline{\mathrm{SIF}}$, which is defined as

$$\text{PAR-weighted}\,\overline{\mathrm{SIF}} = \frac{1}{N}\sum_{\mathrm{day}=1}^{N}\overline{\mathrm{PAR}}_{\mathrm{day}} \times \frac{1}{n}\sum_{\mathrm{day}=1}^{n}\left(\mathrm{SIF}_{t_m} \times \mathrm{DC}_{\mathrm{total}}\right)_{\mathrm{day}} / \overline{\mathrm{PAR}}_{\mathrm{day}}, \tag{5a}$$

$$\text{arithmetic}\,\overline{\mathrm{SIF}} = \frac{1}{n}\sum_{\mathrm{day}=1}^{n}\left(\mathrm{SIF}_{t_m} \times \mathrm{DC}_{\mathrm{total}}\right)_{\mathrm{day}}, \tag{5b}$$

where N is the total number of TROPOMI SIF soundings, and n is the number of cloud-filtered soundings.

In Section 4.1.3.2, we quantitatively demonstrate the clear sky bias using the Amazon Forests as an example, which exhibits a strong seasonal cycle in cloudiness as well as heavily debated responses of photosynthesis in the dry season (Saleska et al., 2007; Doughty et al., 2021; Samanta et al., 2010; Saleska et al., 2016; Morton et al., 2014).

2.2. Topographic impact on upscaling SIF_{t_m} to SIF_{dc}

2.2.1. Adjusting PAR according to topography

Previously, we only discussed atmospheric effects that can bias the scaling from instantaneous to daily average SIF. However, the slope and orientation of the surface can dramatically change the diurnal cycle of received radiation, for example in east or west facing slopes, which can have peak diurnal PAR shifted towards the morning and evening, respectively.

In complex terrain, the diurnal cycle of direct PAR received by a surface is not determined by the SZA but by the angle between the incident direct light and the surface normal (Solar Incidence Angle — SIA, Fig. 2a). For example, terrain oriented towards the sun (SIA < SZA) receives substantially more direct light per projected unit area. As a result, complex terrain results in spatially heterogeneous total PAR as well as the ratio of $\mathrm{PAR_{diffuse}}$ and $\mathrm{PAR_{direct}}$. This can even lead to spatial variations in hydro-climate conditions that vegetation acclimates to Bilir et al. (2021), van der Tol et al. (2007) and Kutiel (1992). Therefore, neglecting the topographic impact on PAR can bias $\mathrm{SIF_{dc}}$ as observed from space. Here, we aim to quantify this bias for $\mathrm{SIF_{dc}}$ and validate our correction scheme using reflectances—which are impacted by the same bias—and classical vegetation indices, for which directional effects mostly cancel out.

Table 1
Summary of all DC models used in this study. A glossary of all variables used in this study is in Appendix D.

DC models	Atmospheric effects		Topography	Equation	Results
	Direct PAR	Diffuse PAR			
$\mathrm{DC_{SZA}}$	✗	✗	✗	(2)	
$\mathrm{DC_{direct}}$	✓	✗	✗	(3)	Section 4.1.1
$\mathrm{DC_{total}}$	✓	✓	✗	(4)	Section 4.1.2
$\mathrm{DC_{DEM}}$	✓	✓	✓	(11)	Section 4.2

To evaluate this impact, we add topographic information to the expression of $\mathrm{DC_{total}}$ (Eq. (4)) on a flat surface.

We first correct $\mathrm{PAR_{direct}}$ given the surface inclination angle (β) and azimuth angle (α) using a simple photometric function (Klein, 1977; Teillet et al., 1982):

$$\mathrm{PAR_{direct,DEM,t}} = \mathrm{PAR_{direct,t}}\frac{\cos(\mathrm{SIA})}{\mu_{\mathrm{t}}}\mathcal{H}(\cos(\mathrm{SIA}_t)). \tag{6}$$

Given the geometry in Fig. 2, the SIA can be derived as

$$\mathrm{SIA} = \sin(\mathrm{SZA})\sin(\beta)\cos(\alpha_{\odot} - \alpha) + \mu\cos(\beta), \tag{7}$$

where $\alpha_{\odot}$ is solar azimuth angle (Duffie and Beckman, 2013).

We preserve the expression for $\mathrm{PAR_{diffuse}}$ assuming isotropic diffuse PAR, which is less dependent on surface orientation. Here, we only include self-shading (i.e. if the SIA is larger than 90°, no direct radiation reaches the surface) but ignore shading by mountain ranges in the vicinity. Thus, the total PAR projected on a tilted surface is:

$$\mathrm{PAR_{total,DEM,t}} = \mathrm{PAR_{direct,t}}\frac{\cos(\mathrm{SIA})}{\mu_{\mathrm{t}}}\mathcal{H}(\cos(\mathrm{SIA}_{t_m})) + \mathrm{PAR_{diffuse},t_m}. \tag{8}$$

2.2.2. Validating the topographic adjustment on PAR

To validate this simple topographic adjustment on PAR in Eq. (8), we make use of the fact that measured reflectances experience the same bias if they are not topographically corrected. However, reflectance ratios are not as affected as the bias cancels out in the ratio. Comparing novel indices that might be susceptible to the topography bias against those that are more robust with respect to slope variations thus provide an indirect validation of our correction approach.

We first apply the adjusted PAR to reflectance (R):

$$\mathrm{R_{DEM}} = \mathrm{R} \times \frac{\mathrm{PAR_{direct},t_m} + \mathrm{PAR_{diffuse},t_m}}{\mathrm{PAR_{direct,DEM},t_m} + \mathrm{PAR_{diffuse},t_m}}, \tag{9}$$

where $\mathrm{R_{DEM}}$ is the topographically corrected R (if the surface slope was neglected during retrievals).

To intuitively interpret the topographic adjustment on PAR, we compare the Vegetation Indices (VIs) built with $\mathrm{R_{DEM}}$ against R in Section 4.2. We choose VIs that are proxies for the greenness of canopy, which varies across slopes, because spatially heterogeneous energy and hydrological conditions in complex terrain cause spatial variations of vegetation distribution (Bilir et al., 2021; van der Tol et al., 2007; Kutiel, 1992). Thus, the difference across VIs and topographically corrected VIs are easy to observe in the context of topography. In this study, we consider the Normalized Difference Vegetation Index (NDVI; Silleos et al. 2006), kernel-based NDVI (Camps-Valls et al., 2021), and $\mathrm{NIR_v}$ (Badgley et al., 2017):

$$\mathrm{NDVI} = \frac{R_{\mathrm{nir}} - R_{\mathrm{red}}}{R_{\mathrm{nir}} + R_{\mathrm{red}}}, \tag{10a}$$

$$\mathrm{kNDVI} = \tanh(\mathrm{NDVI}^2), \tag{10b}$$

$$\mathrm{NIR_v} = \mathrm{NDVI} \times R_{\mathrm{nir}}, \tag{10c}$$

where R_{nir} and R_{red} are near-infrared reflectance and red reflectance.

For band-ratio VIs like NDVI and kNDVI, the corrections should be negligible as measured reflected radiance in the red and NIR spectral

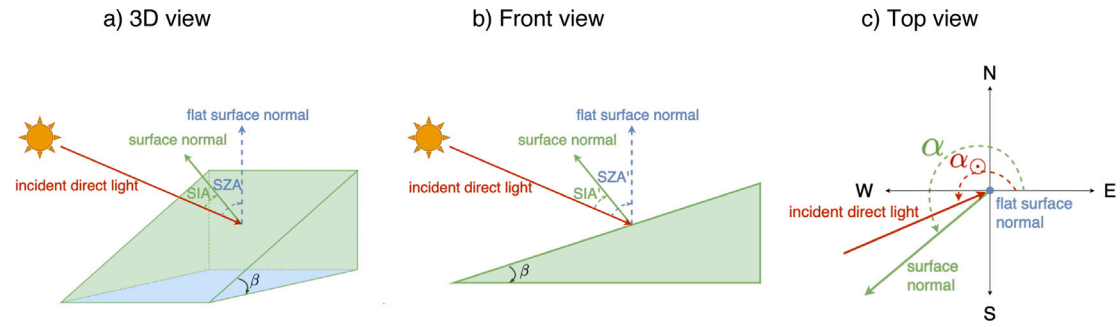

Fig. 2. The Solar Incidence Angle (SIA) and Solar Zenith Angle (SZA) are not equivalent on a tilted slope as demonstrated in (a) a 3D view, (b) a front view, and (c) a top view. SIA is the angle between the incident direct light and the tilted surface normal. SZA is the angle between the incident direct light and flat surface normal. SIA' and SZA' are the projection of SIA and SZA on the front view, respectively. $\alpha_\odot$, β, and α are solar azimuth angle, surface inclination, and surface azimuth, respectively.

bands are affected similarly by surface slope changes, because atmospheric scattering is similar in both bands. It is a valid assumption as both bands are spectrally nearby and only mildly impacted (less than 5%; Fig. 9) by Rayleigh scattering (Bates, 1984).

However, for more complex VIs such as the NIR_V or the Enhanced Vegetation Index (Xiao et al., 2003), the effect of surface slopes does not cancel out. For NIR_V, the effect is directly proportional to the bias in the derived R_{nir}, which is why we focus on the simple NIR_V correction here, as it provides an analogue to our assumptions for the SIF correction. Also because both NIR_V and SIF are primarily driven by fPAR (Badgley et al., 2017; Magney et al., 2020; Mohammed et al., 2019; Joiner et al., 2020; Lin et al., 2019), correcting NIR_V serves as an indirect validation of the SIF validation.

2.2.3. Topographic adjustment on upscaling SIF_{t_m} to SIF_{dc}

The only difference between our topographic correction on R and DC is that the R correction considers PAR at t_m only, while the DC correction requires the full diurnal cycle of PAR. This is because reflectance-based VIs are related to intrinsic properties of the canopy, such as the potential photosynthesis (Silleos et al., 2006; Badgley et al., 2017; Xiao et al., 2003; Camps-Valls et al., 2021).

We derive a Digital Elevation Model (DEM) based length-of-day correction DC_{DEM} as:

$$DC_{DEM} = \frac{1}{\left(PAR_{direct,DEM,t_m} + PAR_{diffuse,t_m}\right)} \times \int_{t_m\text{-}12h}^{t_m+12h} \left(PAR_{direct,\ DEM,t} + PAR_{diffuse,t}\right) dt \quad (11)$$

To focus on the topographic impact, we only use clear-sky PAR to explicitly express DC_{DEM}. The difference between DC_{DEM} and DC_{total} reflects the topographic impact on SIF_{dc}

In Section 4.2, we use the San Gabriel Mountains in California as an example to evaluate the topographic impact on SIF_{dc} aggregated across various sensor footprints. The strong radiation contrast between north and south facing slopes in the San Gabriel Mountains make this region an ideal study site.

3. Data

3.1. Global PAR data

Because there is lack of global-scale ground observation of PAR, we utilize global reanalysis radiation data from the ECMWF ReAnalysis (ERA5), which assimilate various available observations. ERA5 data have been validated independently and enable us to perform a much more thorough analysis than any other dataset (Babar et al., 2019; Urraca et al., 2018; Yang and Bright, 2020). We calculate PAR as a fixed fraction (0.46) of the direct and diffuse surface downwelling shortwave radiation (Zhang et al., 2020; Howell et al., 1983) obtained from ERA5 hourly data in 2020 at 0.5° × 0.5° spatial resolution (Albergel et al., 2018). ERA5 simulates downwelling shortwave radiation at the surface both with clouds (all-sky conditions) and without clouds (clear-sky conditions). In both cases, the ERA5 simulation uses the exact same atmospheric conditions, such as temperature, humidity, ozone, trace gases and aerosols (Muñoz-Sabater et al., 2021). Therefore, we can differentiate the atmospheric impact under clear-sky and all-sky conditions. The ERA5 variables are listed in Appendix B.

For the integrals in the DC expressions (Eqs. (3), (4), and (11)), we interpolate hourly PAR data to 10-min time steps using cubic splines, focusing on land pixels only.

3.2. Solar angles

Given t_m, longitude, and latitude of a surface point, Solar Zenith Angle (SZA) and Solar Azimuth Angle ($\alpha_\odot$) are calculated using the PyEphem astronomy tool (https://github.com/brandon-rhodes/pyephem), which provides the exact Sun–Earth geometry at a given time using orbital characteristics.

We obtain surface elevation (in meters; Fig. 7a) from the NASA Shuttle Radar Topography Mission (SRTM) version 3 with 30-m spatial resolution (NASA JPL, 2013). The inclination angle (β) and azimuth angle (α) of surface pixels (Fig. 7b and c) are calculated from the surface elevation using the hill shading algorithm (Horn, 1981) implemented in RichDEM (Barnes, 2016). With SZA, $\alpha_\odot$, β, and α, we then calculate SIA using Eq. (7).

3.3. SIF data

We use the TROPOMI SIF data described in Köhler et al. (2018) for our analysis because TROPOMI provides a fine spatial and temporal resolution (Köhler et al., 2018) and a much higher sampling frequency compared to all current satellites that are capable of retrieving SIF. The wide swaths with viewing angles of up to 60° allow for a near-daily global coverage. In this study, we use two levels of processed TROPOMI SIF products: (1) instantaneous SIF from individual soundings; and (2) gridded SIF with a temporal resolution of 16 days and a spatial resolution of 0.0833° × 0.0833°, which is aggregated from individual SIF measurements in 2020. We grid all unfiltered TROPOMI soundings as well as the filtered data with cloud fractions smaller than 0.8, which also includes additional retrieval quality filter criteria and is the suggested standard filter for public use of SIF data (Köhler et al., 2018). We then compute the number of averaged soundings per grid cell in both cloud-filtered (n) and unfiltered (N) cases, the latter of which represents the total number of potential TROPOMI soundings. We then evaluate the measurement yield in each grid, defined as the fraction of measurements that passed the cloud filter (the ratio of n to N), as a function of space and time.

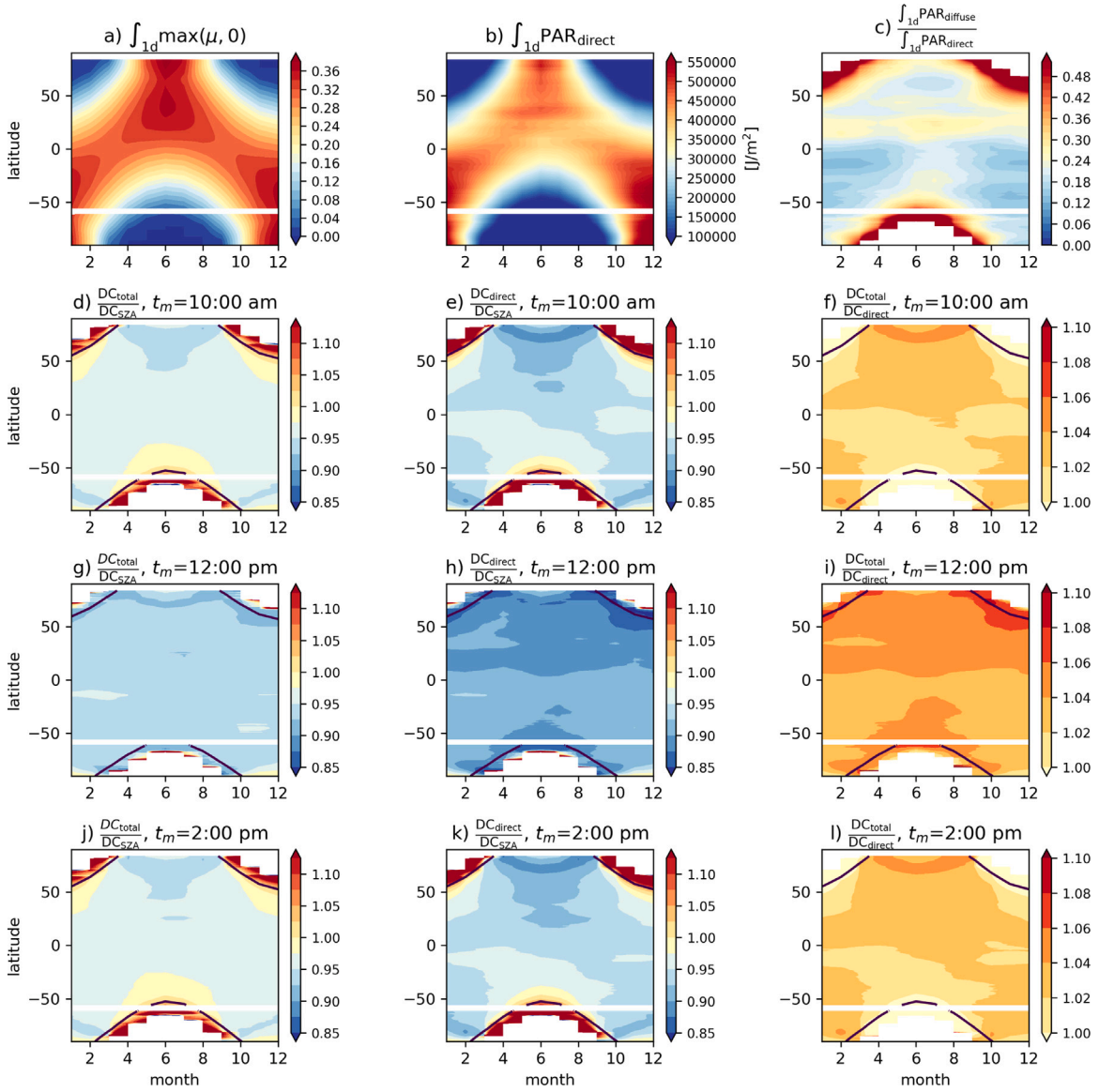

Fig. 3. The zonal-mean impact of atmospheric extinction and $PAR_{diffuse}$ on DC calculation under clear-sky conditions. DCs are calculated using clear-sky PAR. Zonal means are calculated from land pixels only. Panels a and b show the daily integral of μ and PAR_{direct} during daytime. Panel c is the daily integral of $PAR_{diffuse}$ relative to PAR_{direct}. The ratio of DC_{total} to DC_{SZA} (panels d, g, and j) underscores the total impact of atmospheric extinction and $PAR_{diffuse}$. The ratio of DC_{direct} to DC_{SZA} (panels e, h, and k) isolates the impact of atmospheric extinction. The ratio of DC_{total} to DC_{direct} (panels f, i, l) isolates the impact of $PAR_{diffuse}$. Panels d–f assume the overpass time is 10 am Local Solar Time (LST). Panels g–i assume the overpass time is at local noon. Panels j–l assume the overpass time is 2 pm LST. The black lines are the contour of SZA = 80° at t_m. SZA is greater than 80 ° north (south) of the contour in Northern (Southern) Hemisphere.

3.4. Reflectance data

We use R from LandSat Collection 2 Level 2 data (30-m spatial resolution) on July 3, 2020. The mean LandSat t_m in the San Gabriel Mountains is 10:31 am Local Solar Time (LST) when SZA and $\alpha_{\odot}$ are 22.5° and 335.4°, respectively. The azimuth angle is measured in degrees counter-clockwise from East. Then, the grids of R and surface elevation products are matched and transformed to degrees using the Geospatial Data Abstraction Library (GDAL; https://gdal.org), while the 30-m spatial resolution is preserved.

4. Results

Here, we discuss the impact of atmospheric variations on DC, both for scaling from instantaneous SIF to daily averages as well as aggregating daily SIF averages to longer-term temporal averages. The impact of topography is discussed separately.

4.1. Atmospheric effects

4.1.1. Atmospheric effects on DC under clear-sky conditions

For clear-sky conditions, we first examine the validity of the simple approximation used in DC_{SZA}, where the diurnal cycle of PAR is approximated geometrically by μ. Fig. 3a shows that the zonal-mean daily integral of $\mu\mathcal{H}(\mu)$ is a smooth function of time and latitude, and the spatiotemporal pattern is consistent with the daily integral of PAR_{direct} computed from ERA5 in Fig. 3b. The consistency confirms that DC_{SZA} mainly accounts for the diurnal cycle in PAR_{direct}, as expected from a geometric scaling using μ. $PAR_{diffuse}$ is much smaller than PAR_{direct} (Fig. 3c) in most cases (especially for valid solar angles) and thus has no large impact for clear-sky conditions.

DC_{total} derived from the sum of PAR_{direct} and $PAR_{diffuse}$ (Eq. (4)) is smaller than DC_{SZA} but only by less than 10% assuming a t_m at noon local time (Fig. 3g). More importantly, the atmospheric impact on DC_{total}/DC_{SZA} (left column in Fig. 3) is homogeneous across latitudes

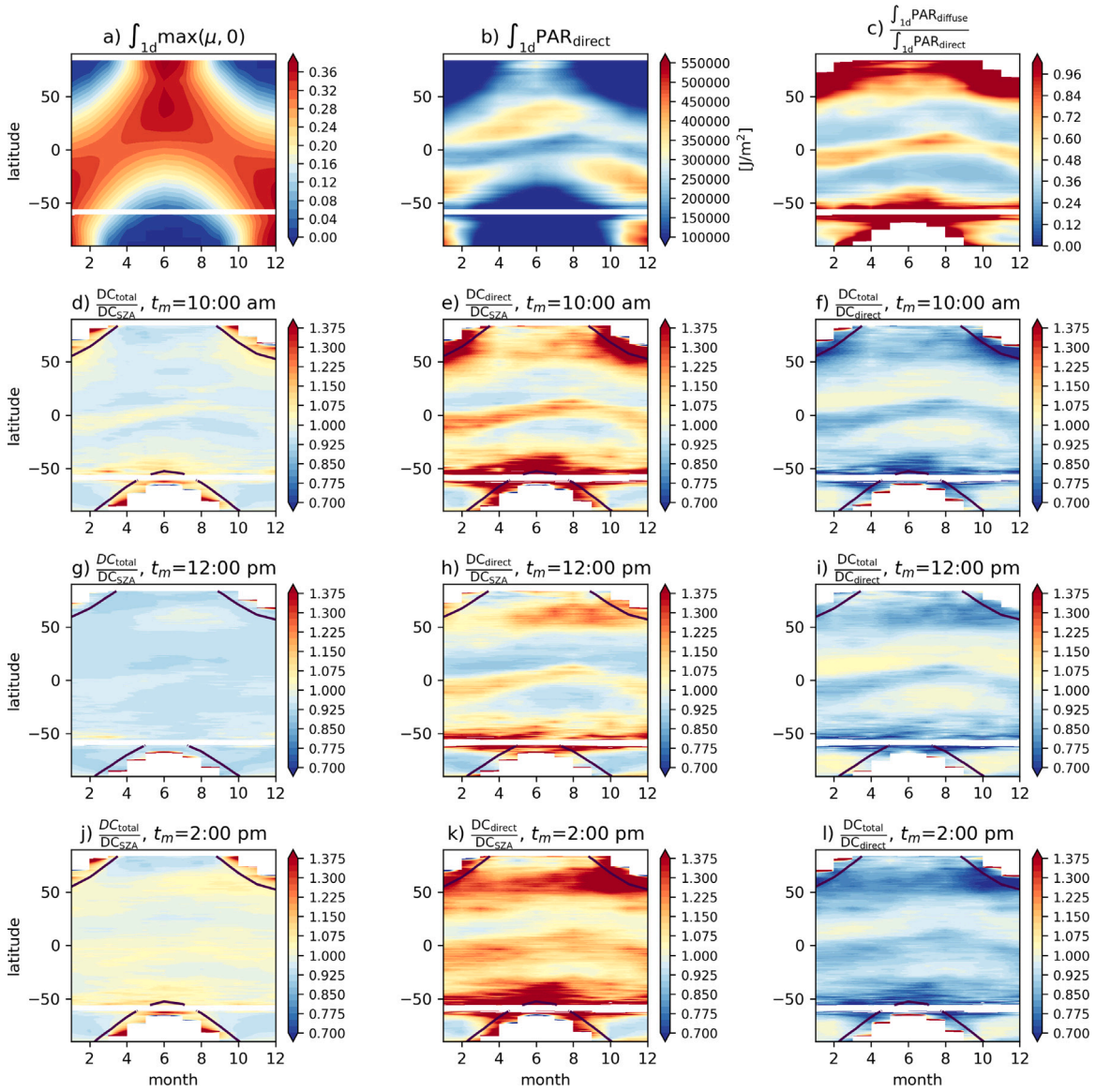

Fig. 4. The zonal-mean impact of atmospheric extinction and $PAR_{diffuse}$ on DC calculation under all-sky conditions. DCs are calculated using all-sky PAR. Zonal means are calculated from land pixels only. Panels a and b show the daily integral of μ and PAR_{direct} during daytime. Panel c is the daily integral of $PAR_{diffuse}$ relative to PAR_{direct}. The ratio of DC_{total} to DC_{SZA} (panels d, g, and j) underscores the total impact of atmospheric extinction and $PAR_{diffuse}$. The ratio of DC_{direct} to DC_{SZA} (panels e, h, and k) isolates the impact of atmospheric extinction. The ratio of DC_{total} to DC_{direct} (panels f, i, and l) isolates the impact of $PAR_{diffuse}$. Panels d–f assume the overpass time is 10 am LST. Panels g–i assume the overpass time is at local noon. Panels j–l assume the overpass time is 2 pm LST. The black lines are the contour of SZA = 80° at t_m. SZA is greater than 80° north (south) of the contour in Northern (Southern) Hemisphere.

and seasons, underlining that the simple geometric correction is not creating spatially varying biases. For DC_{direct}/DC_{SZA} (center column in Fig. 3), the patterns and amplitudes are similar to DC_{total}/DC_{SZA} but have somewhat more absolute variations and spatio-temporal variations. This can only be explained by atmospheric aerosols in ERA5, which can reduce direct and increase diffuse radiation, thus leading to partial compensation in total PAR. Adding $PAR_{diffuse}$ to DC_{direct} has an opposite but smaller impact (Fig. 3i) since $PAR_{diffuse}$ is larger for longer light paths, which partially cancels out the error from ignoring atmospheric extinction in the SZA approximation of PAR_{direct}. It should be mentioned that although the impact of $PAR_{diffuse}$ can be more extreme at high latitudes during winter, SIF soundings are typically filtered out due to limited light intensity when the SZA at t_m is greater than 80°(regions north or south of the black lines in Fig. 3d–i).

The magnitude of biases in DC_{SZA}, compared against DC_{total}, depends on t_m as well. The ratio of DC_{total} to DC_{SZA} is less than 5% (Fig. 3d and j) when t_m is 10 am or 2 pm Local Solar Time (LST). As 10 am and 2 pm are both about two hours away from local solar noon, local PAR is almost identical at these times under clear-sky conditions. Hence, Figs. 3d–f and Figs. 3j–l are symmetric. Overall, the errors in the simple DC_{SZA} approach when compared to using ERA5 PAR data (DC_{total}) in clear sky conditions are surprisingly small (< 10%) and can likely be ignored.

4.1.2. *Atmospheric effects on DC under all-sky conditions*

To show the impact of clouds on DC, we repeat the calculations of DC_{total} and DC_{direct} as shown before with all-sky conditions. As expected, in all-sky conditions PAR_{direct} is lower (Fig. 4b) while $PAR_{diffuse}$ is higher compared to clear-sky conditions. In regions with frequent cloud cover, such as the inter-tropical convergence zone (Fig. 4c), $PAR_{diffuse}$ can often contribute equally to total PAR. Specifically at high latitudes, $PAR_{diffuse}$ is larger than PAR_{direct} due to longer atmospheric light paths. In contrast, $PAR_{diffuse}$ in the subtropics is smaller because of large-scale atmospheric subsidence, resulting in both a dry climate and less frequent cloud cover.

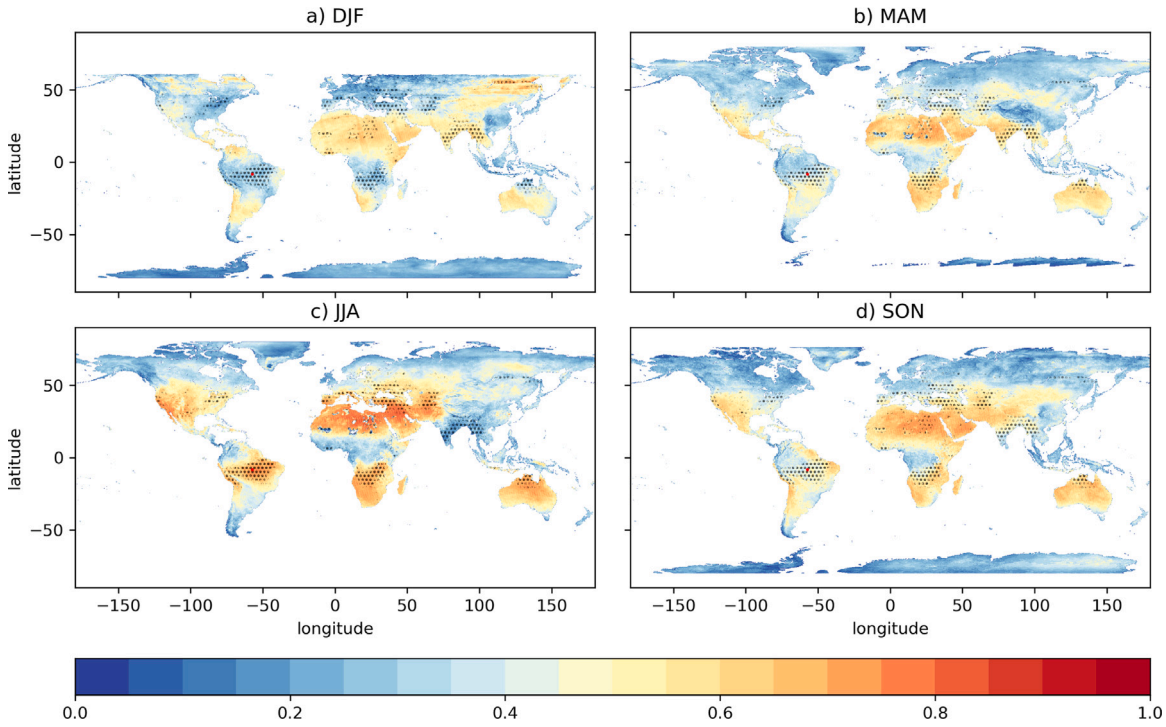

Fig. 5. The seasonal mean measurement yield of SIF soundings, defined as the fraction of measurements that passed the cloud filter (cloud fraction < 0.8), in (a) December, January, and February; (b) March, April, and May; (c) June, July, and August; and (d) September, October, and November. The stippled areas are where the absolute difference between (a) and (c) is larger than 40%. The red star in the Amazon is the location with regional maximum absolute difference between (a) and (c).

There is only a little increase in the overall magnitude of DC_{total}/DC_{SZA} under all sky conditions (Figs. 4d, g, and j) compared to the clear sky case (Figs. 3d, g, and j), even in regions with frequent cloud cover. At first, this is surprising as we expected a much stronger bias in DC_{SZA} under cloudy conditions. If we consider direct light only, the DC_{total}/DC_{SZA} variations are in fact much larger, with strong latitudinal and temporal changes (Figs. 4e, h and k). In regions with the highest discrepancies in DC_{total}/DC_{SZA}, much stronger $PAR_{diffuse}$ due to cloud scattering in all-sky condition contributes more to DC_{total}. As can be seen in Fig. 4f, i and l, the impact of diffuse light can increase the ratio of DC_{total}/DC_{direct} by up to 30% and counteract the variations in DC_{direct}/DC_{SZA}. Hence, the aggregated atmospheric impact (DC_{total}/DC_{SZA}) is more homogeneous across latitudes and time.

Under all-sky conditions, the atmospheric impact on DC is often larger when t_m is 2 pm (Fig. 4j–l), because convective systems often forms clouds in the afternoons when the surface is heated. Thus, unlike in the clear-sky case, Fig. 4d–f and j–i are asymmetric, which can represent an important aspect for comparing satellites with different overpass times.

Overall, this section highlights counteracting effects of scattering for correcting biases in DC_{SZA}. In clear-sky conditions, atmospheric extinction dominates the impact on DC_{total}. In all-sky conditions, $PAR_{diffuse}$ becomes more important, specifically in regions with frequent cloud cover. The simple DC_{SZA} approach is a surprisingly good proxy for DC_{total} in both cases, as overall changes in direct and diffuse PAR negatively co-vary, reducing the bias to less than 10% at coarse spatial and temporal scales.

4.1.3. Effects of cloud filtering on ($\overline{SIF}$) and clear sky biases

When using real satellite data for SIF, we have to take into account that a clear sky sampling bias might exist, which can vary seasonally. Based on reanalysis data, we can evaluate the potential impact and identify regions in which seasonal biases can be most prominent.

4.1.3.1. Spatial patterns of potential clear sky biases.

At the global scale, the measurement yield (n/N) varies spatially and seasonally. The highest seasonal dynamic range in measurement yields occurs in regions with strong seasonal cycles of cloudiness, such as regions with monsoon climate including the Amazon, South of the Sahel, India, and North Australia (stippled area in Fig. 5, indicating > 40% seasonal variations in data yield). These regions with large seasonal variation in SIF measurement yields are potentially subject to seasonally varying clear sky biases.

For high latitudes and non-vegetated areas, such as over ice and desert, the SIF measurement yield is the lowest (Fig. 5) due to high SZAs during the shoulder seasons and polar nights (Fig. C.1). However, the sampling rate during summer months is much better (Fig. C.2) thanks to overlapping ground tracks (incomplete daily coverage occurs between +/- 7deg). These changes in measurement yield at high latitudes are mostly driven by the SZA cutoff and radiance thresholds, hence less prone to clear-sky biases.

4.1.3.2. Quantitative clear sky bias in SIF seasonality.

How large can the clear sky bias actually be over different seasons? Here, we demonstrate the impact of clouds on the SIF seasonality using the Amazon as an example. We use individual TROPOMI measurements falling into a 0.25° × 0.25° box around the location of the red star in Fig. 6a, a region with highly varying data yields (2.75° N, 55.5° W) from March, 2018 to October 2020. The measurement yield can decrease by up to 60% (Fig. 5 and Fig. 6b) during the wet season (shaded periods in Fig. 6a) as fewer soundings pass the cloud filter. PAR-weighted $\overline{SIF}$ is about 25% smaller than the arithmetic mean (Fig. 6c), indicating that $\overline{SIF}$ may be overestimated during periods of frequent cloud cover. Compared to biases in DC, the clear sky bias of > 10% can thus be substantial. The overestimation is more significant when fewer filtered soundings are available.

We compared the arithmetic $\overline{SIF}$ calculated from DC_{total} in the Amazon using all-sky PAR (as in Fig. 4) against clear-sky PAR (as in Fig. 3), which highlights the impact of the diurnal cycle in cloudiness. Although the amplitude of the diurnal cycle biases can be comparable

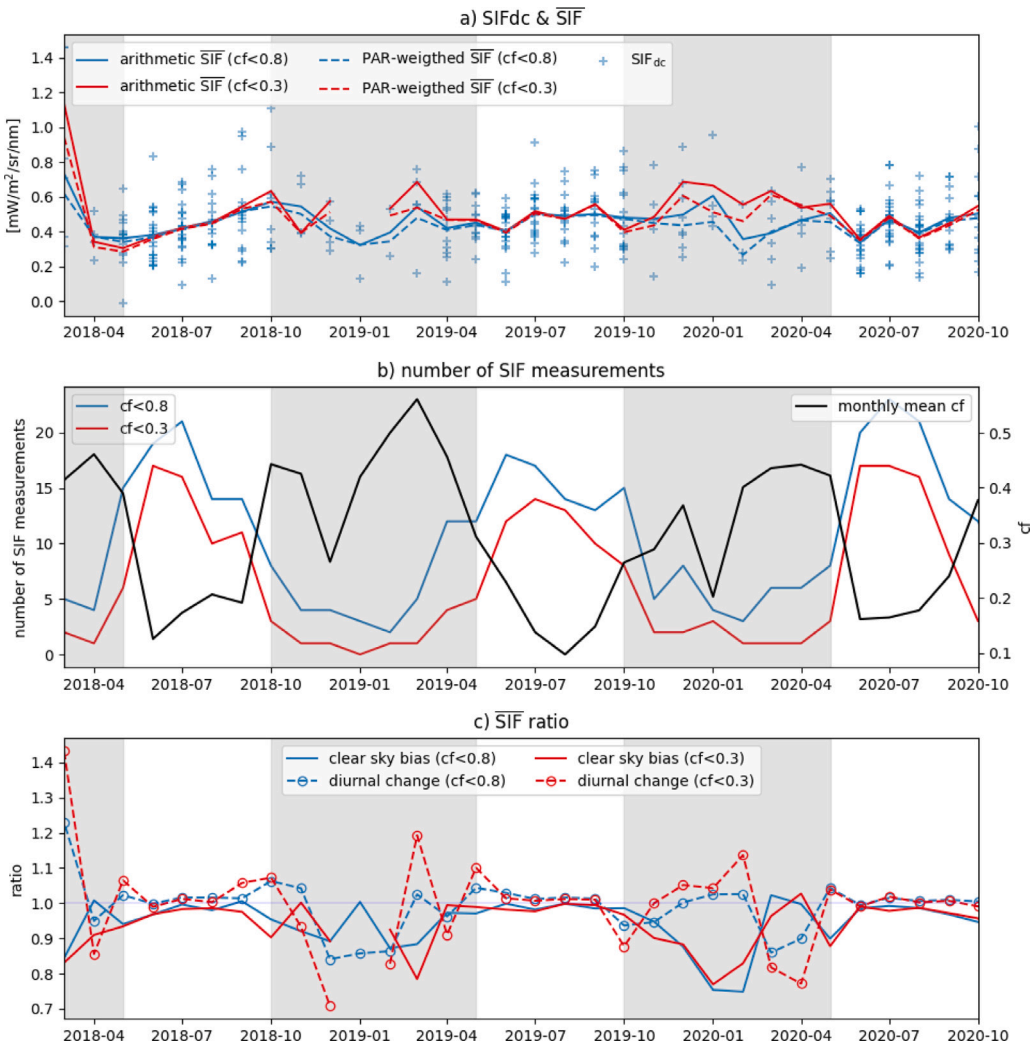

Fig. 6. Impact of clear sky biases on the seasonality of SIF. In panel a, the scatters are the SIF_{dc} of individual soundings, and the lines are arithmetic (solid) and PAR-weighted (dashed) monthly mean SIF ($\overline{SIF}$) filtered by the Cloud Fraction (cf) of 0.8 (blue) and 0.3 (red). Panel b demonstrates the number of SIF measurements filtered by the two cf values, while the black curve is the monthly mean cf. The solid lines in panel c compare the ratio of PAR-weighted $\overline{SIF}$ to arithmetic $\overline{SIF}$ by the two cloud filters. Panel c also compares the impacts of the clear sky bias (solid lines) and diurnal changes in cloudiness discussed in Section 4.1.3 (dashed lines with circles). The impact of clear sky bias is defined as the ratio of PAR-weighted $\overline{SIF}$ to arithmetic $\overline{SIF}$, where DC_{total} is calculated from all-sky PAR for both $\overline{SIF}$. The impact of diurnal changes in cloudiness is evaluated as the ratio of arithmetic $\overline{SIF}$ with DC_{total} calculated by all-sky PAR to clear-sky PAR. The shaded periods are wet seasons with high cf from October to May.

to the clear sky bias, the DC can either be over or underestimated, unlike the consistent overestimation due to the clear sky bias (Fig. 6c). A stricter cloud filter often has a larger impact on SIF_{dc}, suggesting that using a relaxed cloud filter can avoid some of the clear sky bias caused by the diurnal changes in PAR.

Doughty et al. (2021) reported the seasonal dynamic range of the arithmetic $\overline{SIF}$ is only about ± 20% of the annual average in Amazon rain forests. An overestimation of SIF by 25% in wet seasons due to the clear sky bias can cause large biases when interpreting this small season dynamic of $\overline{SIF}$. Therefore, the impact of cloudiness on both DC and upscaling SIF to long-term averages should be considered.

4.2. Topographic effects

4.2.1. Validating the topographic corrections on PAR

The San Gabriel Mountains, California, USA (34°N– 34.6 °N, 118.4 °W – 117.4°W) are located north of the Los Angeles basin and are oriented east–west over 500 km, and their elevation ranges from 0 to more than 2500 m (Fig. 7). The mountains have higher vegetation coverage, inferred from NDVI, kNDVI, and NIR_v, than the north or south of the mountains where deserts and cities are located. In general, the south facing slopes are more barren than north facing slopes (Fig. 8a) because strong radiation increases skin temperature and potential evapotranspiration, which stresses plants in this dry climate.

Before examine the topographically corrected DC, we first validate our topographic correction method on reflectance and VIs (). Our topographic correction has no impact on NDVI and kNDVI, because the correction factor cancels out for both indices. However, the correction changes the NIR_v (Figs. 8i and 9f), which scales with the derived R_{NIR} correction. As the San Gabriel Mountains are very rugged with surfaces facing towards all azimuth directions (Fig. 7d), there are no large-scale features on the map changing dramatically in NIR_v before and after the topographic correction (Fig. 8c and f). However, the NIR_v values of west(east)-facing slopes are higher(lower) after the correction (Fig. 8i).

Fig. 8d–e and g–h show that our topographic correction improves the correlation coefficients (r^2) between NIR_v and NDVI (kNDVI) by 11% (12%) in LandSat pixels where the absolute changes in NIR_v is larger than 0.02. For pixels with smaller changes in NIR_v (between 0.01 and 0.02), the improvements in r^2 are smaller (about 4%). Meanwhile, the root mean squared errors (rmse) are also improved. The correlations of NIR_v with NDVI and kNDVI become nonlinear at high values, which may be attributed to the saturation of NDVI and kNDVI.

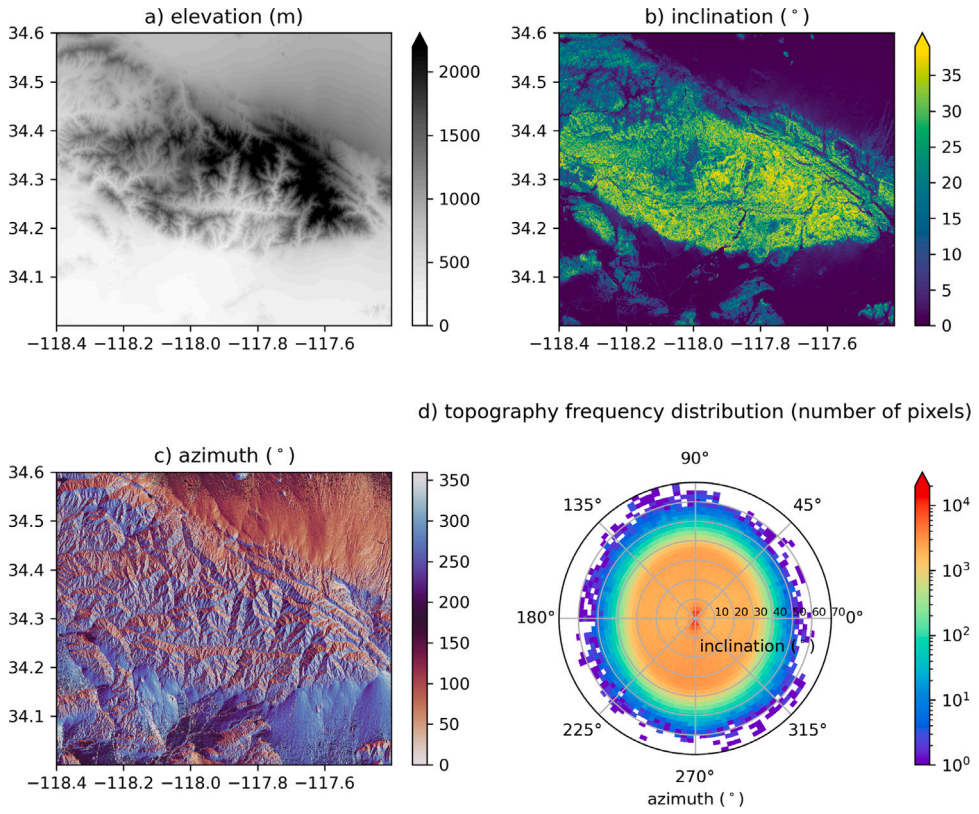

Fig. 7. Surface elevation (a), inclination (b), and azimuth (c) in the San Gabriel Mountains (CA, USA). Panel d shows the frequency distribution of inclination and azimuth from 30-m pixels binned by 2° intervals. Azimuth is measured in degrees counter-clockwise from East.

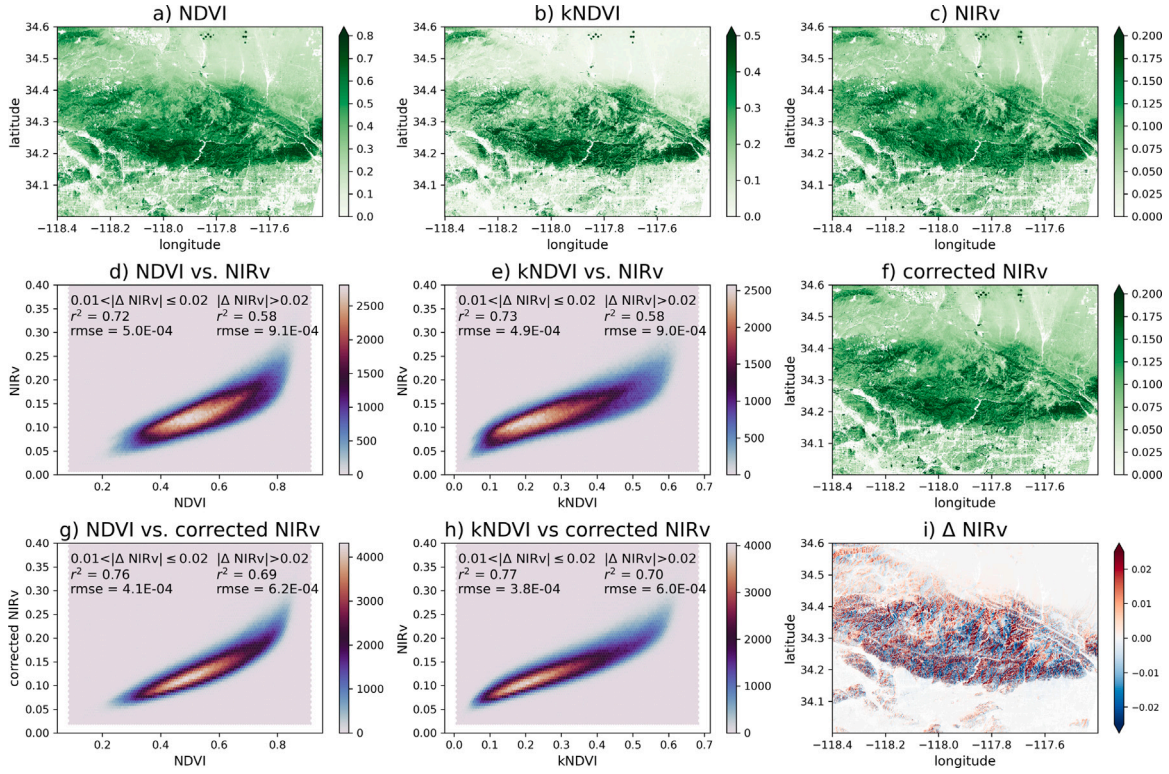

Fig. 8. Impact of topographic correction on surface reflectance using the San Gabriel Mountains (CA, USA) as example, with a LandSat satellite overpass local time t_m of 10:31 am on July 3, 2020. SZA and $\alpha_\odot$ are 22.5° and 335.4°, respectively. Azimuth is measured in degrees counter-clockwise from East. Panels a and b show LandSat based NDVI and kNDVI. Panels c and f are LandSat based NIR_v before and after topographic correction. Panel i is the difference between panels c and f. Panels d and e are the frequency distribution of NIR_v before topographic correction plotted against NDVI and kNDVI. Panels g and h are the frequency distribution of NIR_v after topographic correction plotted against NDVI and kNDVI. In panels d, e, g, and h, the correlation coefficients (r^2) and root mean squared error (rmse) are grouped by absolute difference in NIR_v before and after the topographic correction.

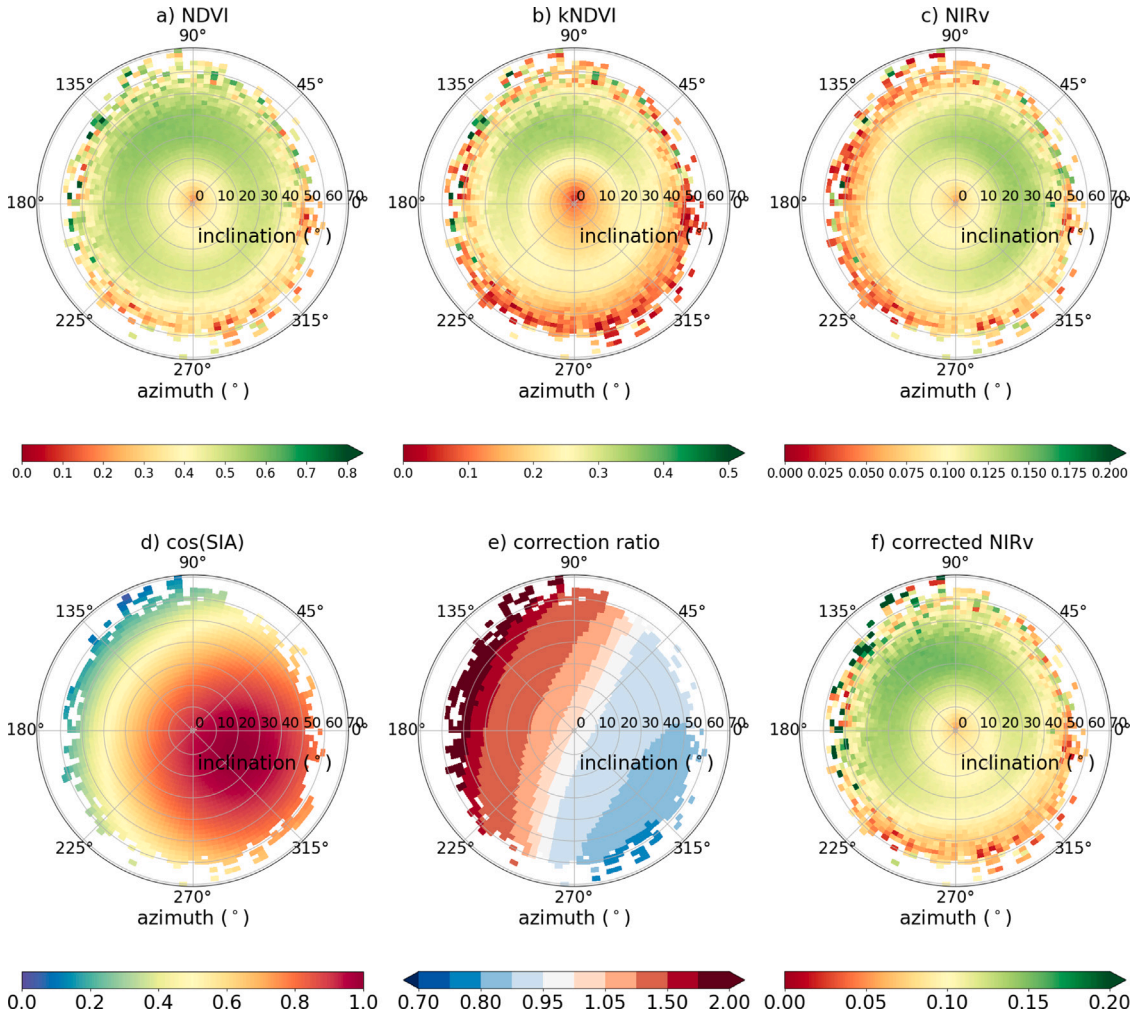

Fig. 9. Impact of topographic correction on surface reflectance in polar maps using the San Gabriel Mountains (CA, USA) as example, with a LandSat satellite overpass local time t_m of 10:31 am on July 3, 2020. SZA and $\alpha_\odot$ are 22.5° and 335.4°, respectively. Azimuth is measured in degrees counter-clockwise from East. Panels a–c and f are the same as Fig. 8a–c and f but in polar coordinates. Surface inclination is on the diameter axis, and surface azimuth is on the angular axis. the cosine of SIA is shown in panel d. Panel e is the ratio of panel f to panel c.

In general, NDVI and kNDVI are higher on northwest facing slopes (Fig. 9a–b), showing a clear preference for vegetation in a dry environment such as Los Angeles. Because the Sun is due East ($\alpha_\odot$ is 335.1°) at the time of the LandSat overpass, east facing slopes have a smaller SIA (Fig. 9d) and receive more direct PAR. Therefore, raw NIR_v is higher on east facing slopes (Fig. 9c). Our topographic correction decreases NIR_v on southeast facing (sun facing in the morning) slopes and increases NIR_v on the northwest facing (sun shaded in the morning) slopes (Fig. 9e).

Using NIR_v without topographic corrections could result in a wrong interpretation as to which surface slopes are more vegetated, as shown in the stark differences between panels a and c in Fig. 9. While the NIR_v has shown a better correspondence with gross primary production (Badgley et al., 2017), one has to keep this potential bias in mind, as the NIR_v looses one key advantage of the NDVI, namely that many error sources cancel out in simple ratio approaches (Frankenberg et al., 2021).

After the topographic correction, all three VIs are higher on northwest facing slopes (Fig. 9a, b, and f), providing a consistent representation of vegetation distribution as a function of surface orientation. Our topographic correction is also comparable to a rigorous semi-empirical modified cosine correction (Soenen et al., 2005; Teillet et al., 1982)(Appendix A) proving that our general approach to correct PAR_{direct} (Eq. (6)) can properly account for the various illumination conditions due to topography. Therefore, we can apply the topographic adjustment to the DC_{DEM} calculation.

4.2.2. Topographic effects on DC

When calculating DC_{DEM}, we consider the different t_m and spatial resolutions from TROPOMI and the upcoming Fluorescence EXplorer (FLEX) mission. TROPOMI overpasses the San Gabriel Mountains at 1:29 pm LST on July 3, 2020, when SZA and $\alpha_\odot$ are 22.6° and 204.6°, respectively. FLEX has a prospective t_m at 10:00 am LST (Drusch et al., 2017), when the SZA and $\alpha_\odot$ are 27.9° and 343.7°. The spatial resolution of TROPOMI is 5 km × 3.5 km at nadir (up to 14 km at the edges of the swath) (Köhler et al., 2018). The prospective spatial resolution of FLEX is 300 × 300 m^2. We first calculate DC_{dem} at the 30-m DEM resolution and then aggregate DC_{DEM} to the spatial resolutions of TROPOMI and FLEX using LandSat NDVI as weights. Here, we neglect topographic impact on the canopy structure, as we focus on the first-order effect of topography, i.e. the amount of light reaching an inclined surface area, and quantitatively analyze this effect against completely neglecting the surface slops.

DEM_{total} is homogeneous in the San Gabriel Mountains because Eq. (4) omits the surface inclination and azimuth. However, DC_{DEM} calculated with Eq. (11) is a function of inclination and azimuth angles as well as t_m. The theoretical ratio of DC_{DEM} to DC_{total} is demonstrated in Fig. 10b and e. The overall magnitude of the theoretical DC_{DEM}

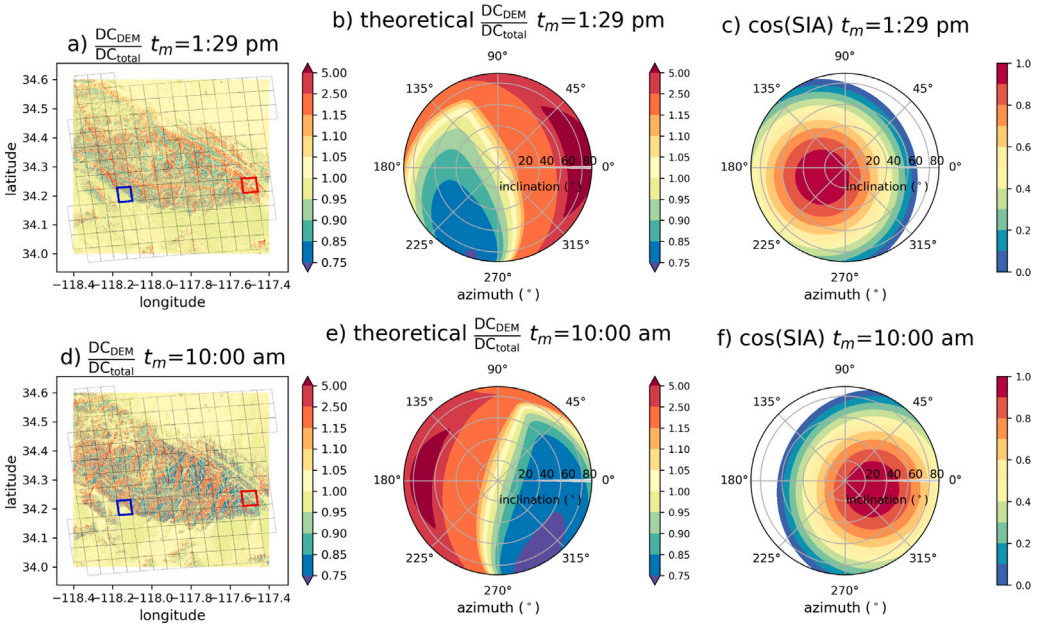

Fig. 10. Topographic corrections on DC with various t_m in San Gabriel Mountains. Panels a–c are the ratio of DC_{DEM} to DC_{total}, the ratio of theoretical DC_{DEM} to DC_{total}, and cosine of SIA at t_m of TROPOMI at 1:29 pm LST on July 3, 2020, when SZA and $\alpha_{\odot}$ are 22.6° and 204.6°, respectively. Azimuth is measured in degrees counter-clockwise from East. Panel d–f are the same as a–c but at the prospective overpass of FLEX at 10:00 am LST, when SZA and $\alpha_{\odot}$ are 27.9° and 343.7°. Panels b, c, e, and f are in polar coordinates, if the surface inclination is from 0–90 °, and the surface azimuth is from 0–360 °. The surface inclination is on the diameter axis, and surface azimuth is on the angular axis. The grids in panels a and d are TROPOMI footprints, where the footprints with maximum and minimum NDVI-weighted $\frac{DC_{DEM}}{DC_{total}}$ are plotted in red and blue, respectively.

can be as large as 500% of DC_{total} (Fig. 10b and e) at the 30-m DEM resolution. These extremely large corrections can happen when the SIA approaches or exceeds 90°, at which only a very low amount of direct PAR reaches the respective surface.

The pattern and amplitude of DC_{DEM} also depend on t_m. When TROPOMI overpasses the San Gabriel Mountains, the northeast facing (sun-shaded) slopes have higher DC_{DEM} than the southwest facing (sun-facing in the afternoon) slopes (Fig. 10b and c). Other sensors may overpass the same region at different t_m resulting in different patterns and magnitudes in DC_{DEM}. For example, when FLEX overpasses 10:00 am LST, the northwest facing (sun-shaded in the morning) slopes have higher DC_{DEM} than the southeast facing (sun-facing) slopes (Fig. 10e and f).

For SIF observed from satellites, the topographic impact on DC is aggregated among the sub-pixels within satellite footprints. In the San Gabriel Mountains, the topographic dependence of illumination and vegetation distribution covary at the sub-pixel scale. Regions with a larger ratio of DC_{DEM} to DEM_{total} also have higher NDVI at both overpass time (Figs. 11h and 12h). According to Fig. 9, these sub-pixels with high NDVI values mostly face north, as expected in a semi-arid climate. Therefore, to account for the varying vegetation coverage across sub-pixel slopes in the aggregated DC_{DEM} over TROPOMI and FLEX footprints, we average the sub-pixel variations of DC_{DEM} in each footprint by weighting them by NDVI (Deng et al., 2007; Turner et al., 2020).

Our results show that although the full dynamic range of DC_{DEM} at 30-m sub-pixel resolution is 75%–500% of DC_{total} (Fig. 10a–b and d–e), the TROPOMI footprint with the maximum NDVI-weighted mean DC_{DEM} in the scene (red outline) is only 9% larger than DC_{total} (Fig. 11a). On the other extreme, the TROPOMI footprint with the minimum NDVI-weighted mean DC_{DEM} (blue outline) is only 1% larger than DC_{total} (Fig. 12a). The bias dynamic range is thus on the order of about 10% for TROPOMI. The upcoming FLEX mission has a much finer footprint (300 × 300 m^2, Coppo et al. 2017). Thus, for increasingly smaller footprints, such as for FLEX (grids in Figs. 11c–d and 12c–d), a topographic slope correction will become more important.

In summary, if one wants to study vegetation dynamics in mountains, corrections on both SIF and surface reflectance play a crucial role, as otherwise even the greenness variations as a function of surface slope and orientation can be severely misinterpreted. While individual effects of highly tilted surfaces can be substantial, they might be reduced at coarser spatial scales, where mean slopes are smaller. For very rugged terrain like the San Gabriel Mountains, the sub-pixel variations are mostly smoothed out within the comparatively coarse TROPOMI footprint (grids in Fig. 10). Other mountain ranges might have more spatially extended slopes, which could even be important for coarser-scale sensors such as TROPOMI. Overall, biases in the length-of-day correction due to surface slopes are of similar magnitude as the overall atmospheric effects but will become increasingly crucial for high surface slopes and for smaller footprints sizes.

5. Discussion

5.1. Significance of atmosphere on DC

In this study, we use reanalysis PAR data to evaluate the impact of neglected atmospheric extinction in the conventional calculation of DC for SIF. We find that the overall bias in the simple geometric approach that is widely used in SIF studies is surprisingly small, both for cloudy and cloud free conditions. In most case, the bias is smaller than 10% at coarse spatial and temporal scales. The main reason for the small bias is a compensating effect of a reduction in direct light and enhancement of diffuse light when clouds and aerosols are present. To be more accurate, our proposed DC corrections can use actual PAR data from meteorological reanalysis data but in most cases, the simple DC_{SZA} should suffice and our results support the previously unvalidated simple approach to scale instantaneous SIF to daily averages.

5.2. Significance of clear sky bias in temporal averages

When SIF_{dc} is upscaled in time, e.g. to monthly averages, changes in daily PAR within the averaging window should be taken into account, especially in regions with low measurement yields due to frequent

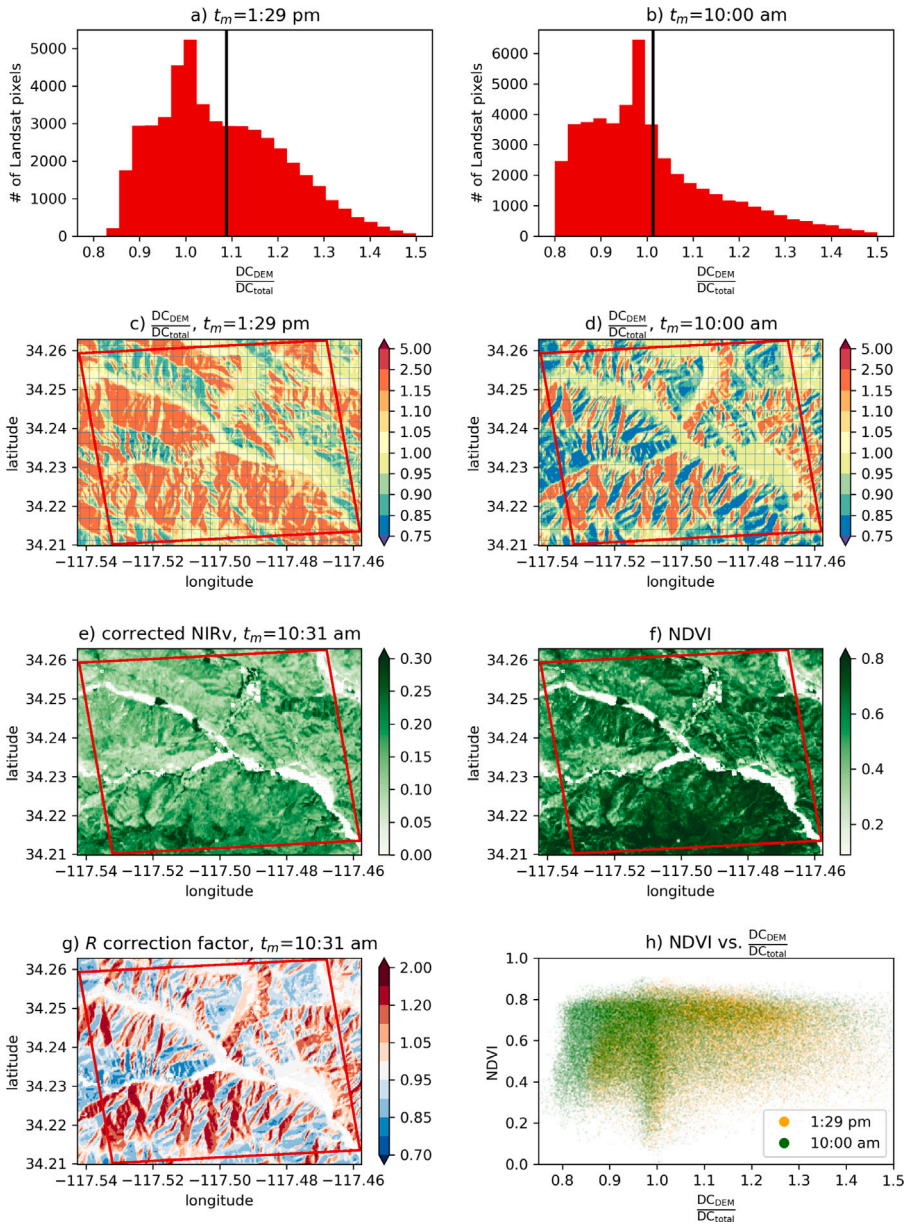

Fig. 11. In the TROPOMI footprint with maximum NDVI-weighted mean $\frac{DC_{DEM}}{DC_{total}}$ (the red outlined footprint in Fig. 10), $\frac{DC_{DEM}}{DC_{total}}$ of all sub-pixels is presented in a histogram (panel a) and a zoomed-in map (panel c) when t_m is at TROPOMI overpass (1:29 pm LST on July 3, 2020). Panels b and d are the same as panels a and c but at prospective FLEX overpass (10:00 am LST on July 3, 2020). The black lines in panels a and b indicate the ratio of NDVI-weighted mean DC_{DEM} to DC_{total} in this TROPOMI footprint. The red frame in all maps depicts actual TROPOMI footprint. The grids in (c) and (d) are the prospective FLEX footprints.

cloud cover. This way, the upscaled monthly SIF is not biased by SIF measurements from clear days only. We find that seasonal clear-sky biases can be on the order of 25% larger than most of the biases in the simple DC correction. While our approach uses just reanalysis data, one might also apply actual PAR measurements at field sites for the correction, if available. However, only reanalysis data can provide corrections for the clear sky bias at global scales.

5.3. Significance of topography on DC

Topography can be an important factor to consider for interpreting satellite measured SIF as well as NIRv in complex terrain because their magnitudes depend on the radiation projected on tilted surfaces. The significance of topographic corrections on SIF and NIRv depends on the relative scale of surface roughness and satellite footprints. For example, the impact of very rugged terrain in San Gabriel Mountains is mostly smoothed out within kilometer-wide TROPOMI footprints, while the topography can be significant in the footprints of upcoming FLEX mission which has 300-wide footprints.

The topographic impact on DC also compounds with the dependence of vegetation distribution on topography. Thus, the heterogeneous vegetation distribution should be considered when aggregating varying sub-pixel DC due to topography. In the meantime, topographically corrected SIF and VIs in fine spatial resolutions can benefit vegetation studies across environmental gradients related to topography, which are restricted by conventional observation tools, such as Eddy Covariance techniques.

5.4. Uncertainties in explicitly expressed DC models

The current calculation for DC_{total} and DC_{DEM} may inherit errors from the reanalysis data. For example, we assume PAR is a constant

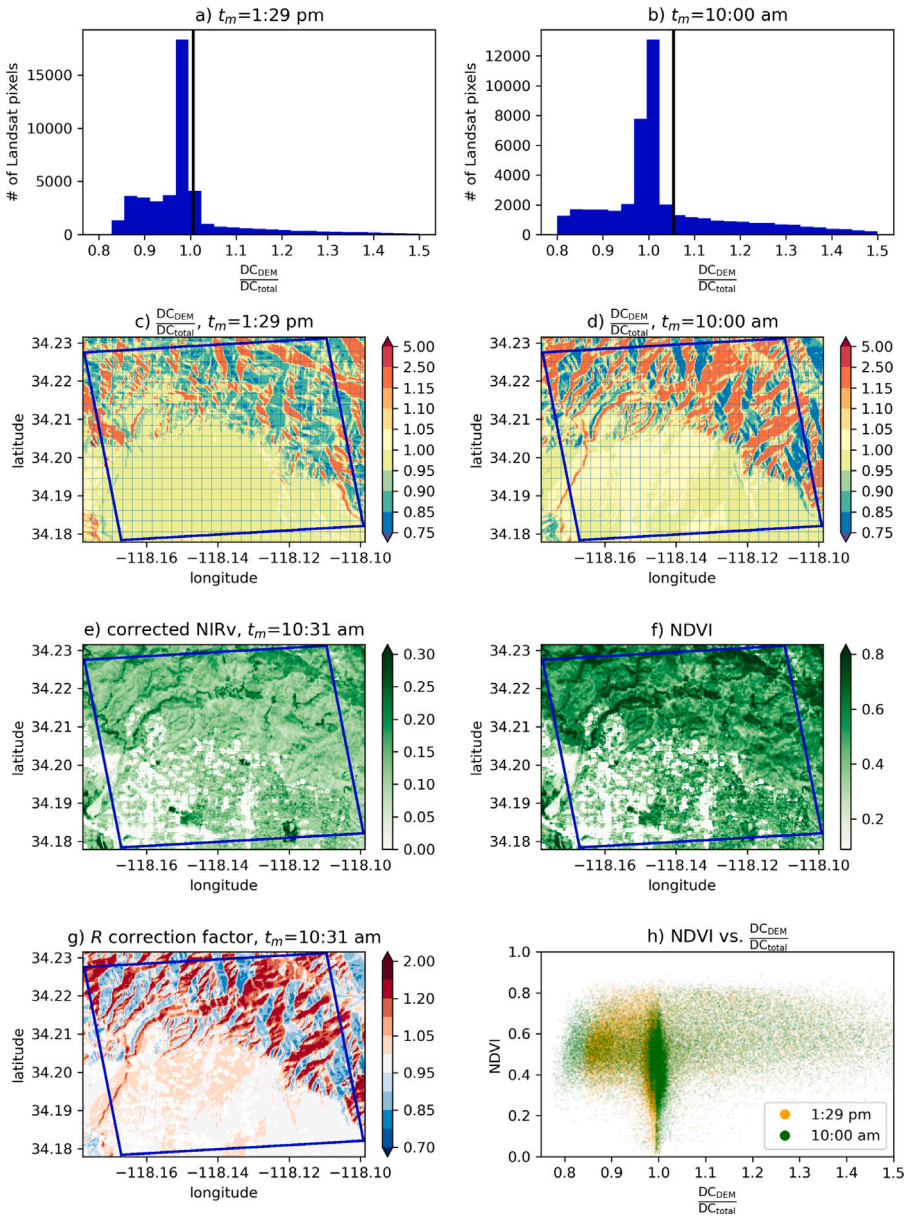

Fig. 12. In the TROPOMI footprint with minimum NDVI-weighted mean $\frac{DC_{DEM}}{DC_{total}}$ (the blue outlined footprint in Fig. 10), $\frac{DC_{DEM}}{DC_{total}}$ of all sub-pixels is presented in a histogram (panel a) and a zoomed-in map (panel c) when t_m is at TROPOMI overpass (1:29 pm LST on July 3, 2020). Panels b and d are the same as panels a and c but at prospective FLEX overpass (10:00 am LST on July 3, 2020). The black lines in panels a and b indicate the ratio of NDVI-weighted mean DC_{DEM} to DC_{total} in this TROPOMI footprint. The blue frame in all maps depicts actual TROPOMI footprint. The grids in (c) and (d) are the prospective FLEX footprints.

fraction of shortwave radiation at the surface since the current ERA5 version does not provide accurate PAR data. The absolute value of this constant is less important here since it is canceled out when calculating DCs. However, this assumption may not hold since the atmospheric scattering along the light path is wavelength dependent (Bates, 1984). Blue light is more sensitive to Rayleigh scattering than longer wavelengths. Under different cloud cover and light path lengths, the spectral shape of incident PAR at the surface can be different from the spectral shape at the top of atmosphere, which would require a scene dependent scaling factor between short-wave totals and PAR. To further improve the accuracy of DCs, accurately calculated PAR data should be used when it is published in future ERA5 versions. In the future, analyzing the uncertainty caused by reanalysis data and validating the result with in-situ PAR data might be needed.

In addition, future corrections might treat direct and diffuse light separately and take into account that GPP can saturate at high PAR levels while SIF is only mildly reduced. A simple non-linear scaling function for PAR in all our correction schemes could takes some of these effects into account but is omitted here as we wanted to focus on potential biases under the most benign assumptions.

6. Conclusion

Instantaneous SIF measurements require correction factors to scale these measurements to daily averages, which can then be aggregated within longer time scales. We focus on three factors impacting daily average SIF and its temporal averages spanning multiple days: atmospheric scattering, clear-sky biases, and topography. Overall, we find that the simple and frequently used DC_{SZA} approach is a convenient yet surprisingly accurate tool for calculating DC on a flat surface, which yields less than 10% biases compared to using exact PAR. In extreme cases, such as a high SZA at t_m and cloudy days, using DC_{SZA} is less accurate for SIF_{dc} and its seasonality since the biases can reach up to 20%.

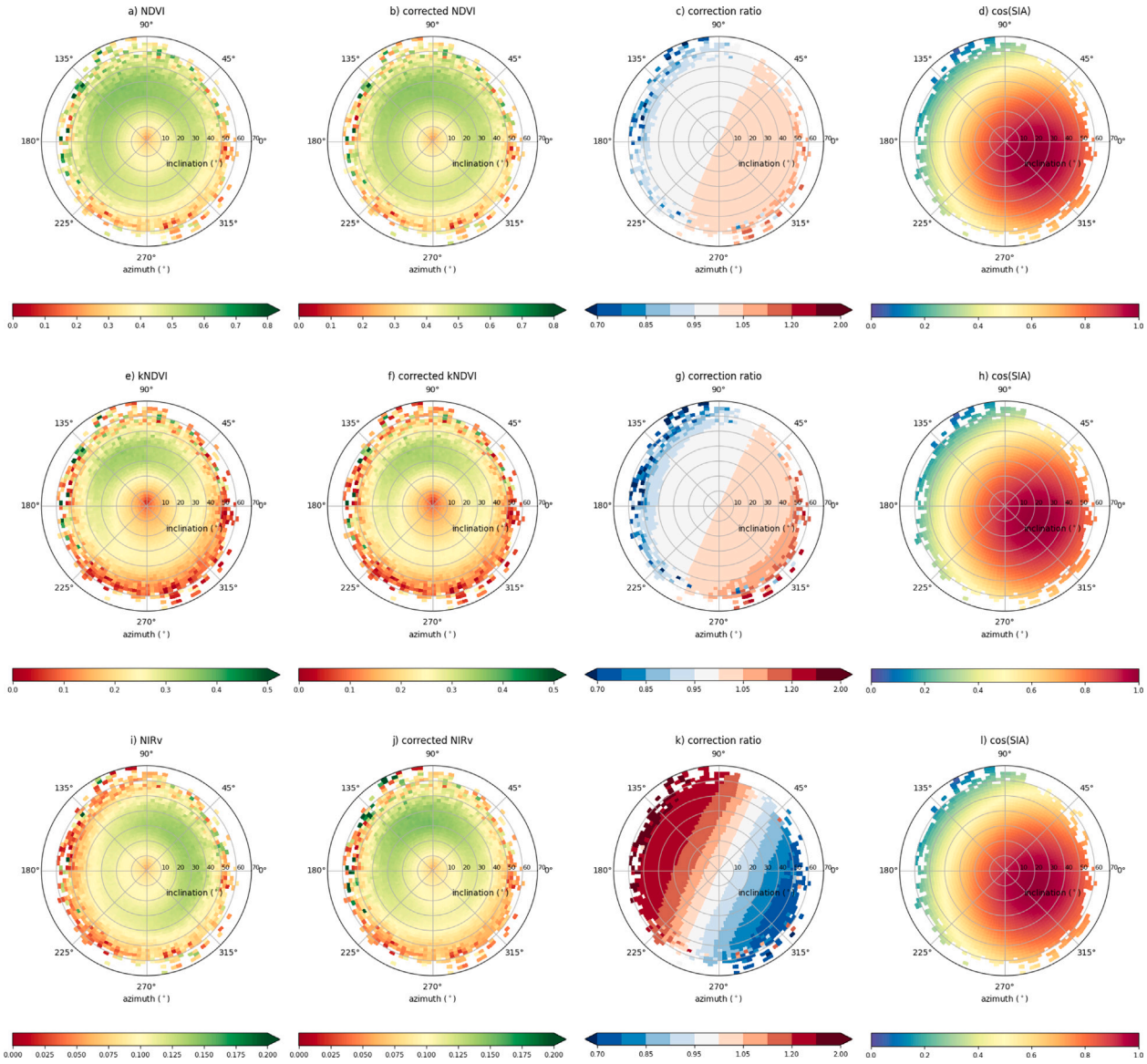

Fig. A.1. (a) original NDVI; (b) topography corrected NDVI; (c) topography corrected NDVI/original NDVI; (d) cos(SZA) at LandSat overpass time (10:31 am on July 3, 2020); (e) original kNDVI; (f) topography corrected kNDVI; (g) topography corrected kNDVI/original kNDVI; (h) same as (d); (i) original NIR_v; (j) topography corrected NIR_v; and (k) topography corrected NIR_v/original NIR_v; and (l) same as (d). In these polar maps, surface slope is on the diameter axis, and surface aspect is on the angle axis.

When aggregating measurements in time, we find that clear-sky biases can arise. For regions experiencing significant seasonal changes in cloudiness, PAR-weighted monthly mean SIF benefits the interpretation of SIF_{dc} seasonality. This can even compound the interpretation of seasonal SIF dynamics that have a low seasonal dynamic range in SIF but large variations in cloudiness. This holds for the Amazon basin in regions with distinct dry and wet seasons, for which SIF in periods with frequent cloudiness can be overestimated by about 25%, which is significant given the overall seasonal dynamic range in SIF is only ±20%.

For complex terrains, we find that an additional correction for surface slopes and orientation is required. Our topographically corrected expression for DC is not negligible, specifically for satellites with small footprints, which can observe highly tilted surfaces within their footprints. In our examples, the biases in DC due to topography can be up to 500% and also impact reflectance measurements, especially the novel NIR_v index.

As more space-borne SIF measurements become available, our length-of-day correction and monthly averaging methods are useful for homogenizing and comparing SIF measurements across a variety of overpass and spatiotemporal scales. In complex terrain, including the topography to the calculation of DC is especially critical for satellites with finer footprints but can also be relevant for coarser spatial scales, e.g. if regions of the size of the satellite footprint are sloped.

Data availability

Data will be made available on request.

Acknowledgments

This research is supported by the NASA CMS, USA (award 80NSSC20K0010) and OCO Science team projects, USA (award 80NSSC18K0895). We use a Julia gridding package from https://github.com/cfranken/gridding.

Appendix A. Cosine correction on VIs

We correct the surface reflectance with a semi-empirical method. For vegetated pixels (NDVI>0.3), we use the Sun-Canopy-Sensor (SCS+C)

Table B.1
The names of variables used in this study and their names in ERA5 products.

Variables used in this study		ERA5 variable names
clear-sky	PAR_{direct}	0.46 × Clear-sky direct solar radiation at surface
	$PAR_{diffuse}$	0.46 × (Surface solar radiation downward, clear sky - Clear-sky direct solar radiation at surface)
all-sky	PAR_{direct}	0.46 × Total sky direct solar radiation at surface
	$PAR_{diffuse}$	0.46 × (Surface solar radiation downwards - Total sky direct solar radiation at surface)

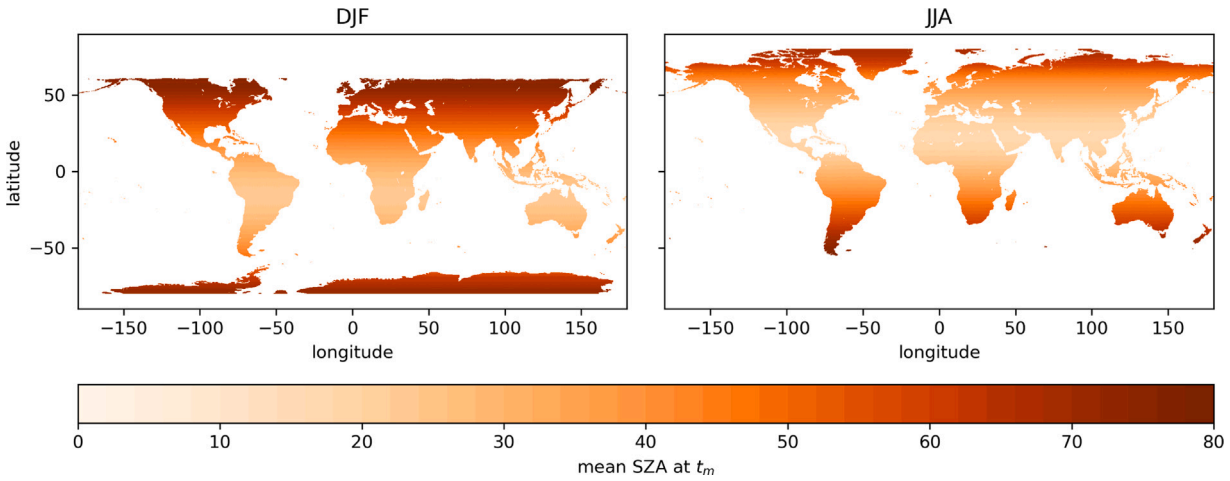

Fig. C.1. The mean SZA at t_m per 16 days averaged over December, January, and February (left panel) and June, July, and August (right panel).

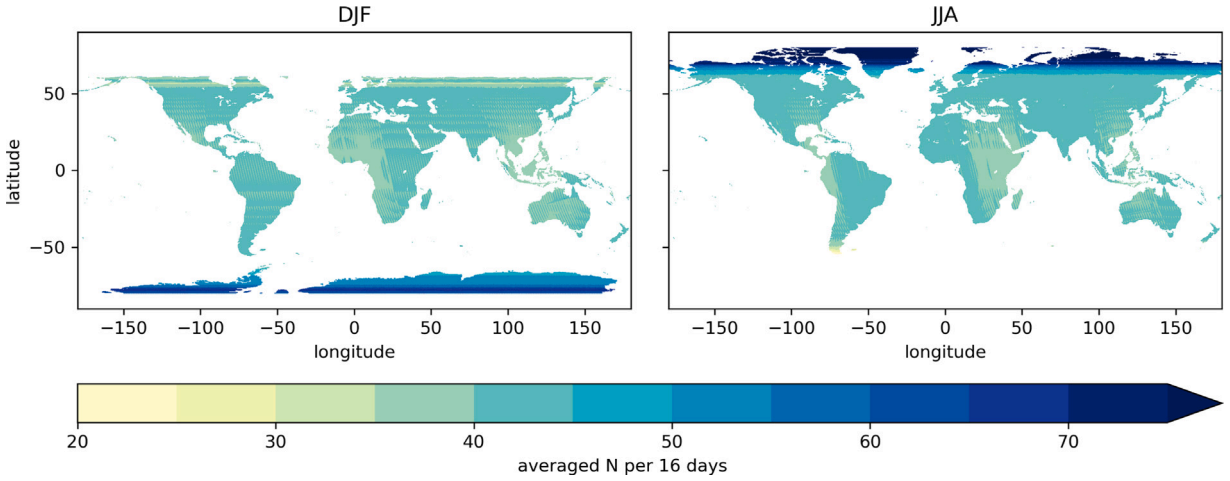

Fig. C.2. The total numbers of unfiltered soundings (N) per 16 days averaged over December, January, and February (left panel) and June, July, and August (right panel).

topographic correction (Soenen et al., 2005). For less-vegetated pixels (NDVI≤0.3), we use the slope-aspect correction (Teillet et al., 1982). The C factor in both corrections were calculated from regressing the surface reflectance and cos(SZA) in less-vegetated pixels. Thus, the C factor is wavelength-dependent. This explains the small changes in NDVI and kNDVI after the correction in Fig. A.1. Overall, the corrected NIR_v using our method (Fig. 9e–f) is very similar to using the semi-empirical correction method for R (Fig. A.1j–k).

Appendix B. Details of calculating PAR_{direct} and $PAR_{diffuse}$ using ERA5 reanalysis data

See Table B.1.

Appendix C. Maximum number of soundings

We use the same gridded SIF product as Section 4.1.3.1, which is aggregated from individual SIF measurements in 2020 and has a temporal resolution of 16 days and a spatial resolution of 0.0833° × 0.0833°. The number of averaged soundings per grid cell is n in cloud-filtered and N in unfiltered cases, the latter of which represents the total number of potential TROPOMI soundings.

The maximum numbers of soundings are higher at high latitudes (Fig. C.2) because of overlapping ground tracks. However, due to larger SZA (Fig. C.1), the measurement yield is smaller at high latitudes (Fig. 5).

Appendix D. List of variables

Acronym	Term
t	Time
t_m	Time of measurement
SZA	Solar zenith angle
$\alpha_\odot$	Solar azimuth angle
μ	Cosine of SZA
β	Surface inclination angle
α	Surface azimuth angle
SIA	Solar incidence angle
SIF_{t_m}	Instantaneous SIF at t_m
SIF_{dc}	Daily-average SIF
PAR	Photosynthetic active radiation
PAR_{direct}	Direct PAR
$PAR_{diffuse}$	Diffuse PAR
DC	Length-of-day correction factor
DC_{SZA}	Conventional DC using cosine SZA
DC_{direct}	DC using PAR_{direct} only
DC_{total}	DC using both PAR_{direct} and $PAR_{diffuse}$
$PAR_{direct,\ DEM}$	Direct PAR corrected by surface topography
DC_{DEM}	DC considering surface topography
R	Reflectance
R_{DEM}	Topographically corrected R
n	Number of cloud-filtered soundings
N	Number of total amount of soundings (before cloud filtering)
$\overline{PAR}_{day}$	Daily mean PAR
$\overline{PAR}_{month}$	Monthly mean PAR
$\overline{SIF}$	Monthly mean SIF

References

Albergel, C., Dutra, E., Munier, S., Calvet, J.-C., Munoz-Sabater, J., de Rosnay, P., Balsamo, G., 2018. ERA-5 and ERA-Interim driven ISBA land surface model simulations: which one performs better? Hydrol. Earth Syst. Sci. 22 (6), 3515–3532. http://dx.doi.org/10.5194/hess-22-3515-2018, URL https://hess.copernicus.org/articles/22/3515/2018/.

Babar, B., Graversen, R., Boström, T., 2019. Solar radiation estimation at high latitudes: Assessment of the CMSAF databases, ASR and ERA5. Sol. Energy 182, 397–411. http://dx.doi.org/10.1016/j.solener.2019.02.058, URL https://linkinghub.elsevier.com/retrieve/pii/S0038092X19301847.

Badgley, G., Field, C.B., Berry, J.A., 2017. Canopy near-infrared reflectance and terrestrial photosynthesis. Sci. Adv. 3 (3), e1602244. http://dx.doi.org/10.1126/sciadv.1602244, URL http://advances.sciencemag.org/lookup/doi/10.1126/sciadv.1602244.

Barnes, R., 2016. R-barnes/richdem. URL https://github.com/r-barnes/richdem original-date: 2013-01-06T15:33:34Z.

Bates, D.R., 1984. Rayleigh scattering by air. Planet. Space Sci. 32 (6), 785–790. http://dx.doi.org/10.1016/0032-0633(84)90102-8, URL https://linkinghub.elsevier.com/retrieve/pii/0032063384901028.

Bilir, T.E., Fung, I., Dawson, T.E., 2021. Slope-Aspect Induced Climate Differences Influence How Water Is Exchanged Between the Land and Atmosphere. J. Geophys. Res. Biogeosci. 126 (5), http://dx.doi.org/10.1029/2020JG006027, URL https://onlinelibrary.wiley.com/doi/10.1029/2020JG006027.

Camps-Valls, G., Campos-Taberner, M., Moreno-Martinez, A., Walther, S., Duveiller, G., Cescatti, A., Mahecha, M.D., Muñoz Marí, J., García-Haro, F.J., Guanter, L., Jung, M., Gamon, J.A., Reichstein, M., Running, S.W., 2021. A unified vegetation index for quantifying the terrestrial biosphere. Sci. Adv. 7 (9), eabc7447. http://dx.doi.org/10.1126/sciadv.abc7447, URL https://advances.sciencemag.org/lookup/doi/10.1126/sciadv.abc7447.

Coppo, P., Taiti, A., Pettinato, L., Francois, M., Taccola, M., Drusch, M., 2017. Fluorescence Imaging Spectrometer (FLORIS) for ESA FLEX Mission. Remote Sens. 9 (7), 649. http://dx.doi.org/10.3390/rs9070649, URL http://www.mdpi.com/2072-4292/9/7/649.

Deng, Y., Chen, X., Chuvieco, E., Warner, T., Wilson, J.P., 2007. Multi-scale linkages between topographic attributes and vegetation indices in a mountainous landscape. Remote Sens. Environ. 111 (1), 122–134. http://dx.doi.org/10.1016/j.rse.2007.03.016, URL https://linkinghub.elsevier.com/retrieve/pii/S0034425707001393.

Doughty, R., Xiao, X., Qin, Y., Wu, X., Zhang, Y., Moore, B., 2021. Small anomalies in dry-season greenness and chlorophyll fluorescence for Amazon moist tropical forests during El Niño and La Niña. Remote Sens. Environ. 253, 112196. http://dx.doi.org/10.1016/j.rse.2020.112196, URL https://linkinghub.elsevier.com/retrieve/pii/S0034425720305691.

Drusch, M., Moreno, J., Del Bello, U., Franco, R., Goulas, Y., Huth, A., Kraft, S., Middleton, E.M., Miglietta, F., Mohammed, G., Nedbal, L., Rascher, U., Schüttemeyer, D., Verhoef, W., 2017. The FLuorescence EXplorer Mission Concept—ESA's Earth Explorer 8. IEEE Trans. Geosci. Remote Sens. 55 (3), 1273–1284. http://dx.doi.org/10.1109/TGRS.2016.2621820.

Duffie, J.A., Beckman, W.A., 2013. Solar engineering of thermal processes / John A. Duffie, William A. Beckman, 4th ed John Wiley, Hoboken.

Frankenberg, C., Fisher, J.B., Worden, J., Badgley, G., Saatchi, S.S., Lee, J.-E., Toon, G.C., Butz, A., Jung, M., Kuze, A., Yokota, T., 2011. New global observations of the terrestrial carbon cycle from GOSAT: Patterns of plant fluorescence with gross primary productivity: Chlorophyll Fluorescence From Space. Geophys. Res. Lett. 38 (17), n/a–n/a. http://dx.doi.org/10.1029/2011GL048738, URL http://doi.wiley.com/10.1029/2011GL048738.

Frankenberg, C., Yin, Y., Byrne, B., He, L., Gentine, P., 2021. Comment on "Recent global decline of CO_2 fertilization effects on vegetation photosynthesis". Science 373 (6562), eabg2947. http://dx.doi.org/10.1126/science.abg2947, URL https://www.science.org/doi/10.1126/science.abg2947.

Gentine, P., Alemohammad, S.H., 2018. Reconstructed Solar-Induced Fluorescence: A Machine Learning Vegetation Product Based on MODIS Surface Reflectance to Reproduce GOME-2 Solar-Induced Fluorescence. Geophys. Res. Lett. 45 (7), 3136–3146. http://dx.doi.org/10.1002/2017GL076294, URL https://onlinelibrary.wiley.com/doi/abs/10.1002/2017GL076294.

Gu, L., Fuentes, J.D., Shugart, H.H., Staebler, R.M., Black, T.A., 1999. Responses of net ecosystem exchanges of carbon dioxide to changes in cloudiness: Results from two North American deciduous forests. J. Geophys. Res.: Atmos. 104 (D24), 31421–31434. http://dx.doi.org/10.1029/1999JD901068, URL http://doi.wiley.com/10.1029/1999JD901068.

Gu, L., Han, J., Wood, J.D., Chang, C.Y.-Y., Sun, Y., 2019. Sun-induced Chl fluorescence and its importance for biophysical modeling of photosynthesis based on light reactions. New Phytol. 223 (3), 1179–1191. http://dx.doi.org/10.1111/nph.15796, URL https://onlinelibrary.wiley.com/doi/10.1111/nph.15796.

He, L., Magney, T., Dutta, D., Yin, Y., Köhler, P., Grossmann, K., Stutz, J., Dold, C., Hatfield, J., Guan, K., Peng, B., Frankenberg, C., 2020. From the Ground to Space: Using Solar-Induced Chlorophyll Fluorescence to Estimate Crop Productivity. Geophys. Res. Lett. 47 (7), http://dx.doi.org/10.1029/2020GL087474, URL https://onlinelibrary.wiley.com/doi/10.1029/2020GL087474.

Horn, B.K.P., 1981. Hill shading and the reflectance map. Proc. IEEE 69 (1), 14–47. http://dx.doi.org/10.1109/PROC.1981.11918, URL http://ieeexplore.ieee.org/document/1456186/.

Howell, T.A., Meek, D.W., Hatfield, J.L., 1983. Relationship of photosynthetically active radiation to shortwave radiation in the San Joaquin Valley. Agric. Meteorol. 28 (2), 157–175. http://dx.doi.org/10.1016/0002-1571(83)90005-5, URL https://linkinghub.elsevier.com/retrieve/pii/0002157183900055.

Hu, J., Liu, L., Guo, J., Du, S., Liu, X., 2018. Upscaling Solar-Induced Chlorophyll Fluorescence from an Instantaneous to Daily Scale Gives an Improved Estimation of the Gross Primary Productivity. Remote Sens. 10 (10), 1663. http://dx.doi.org/10.3390/rs10101663, URL http://www.mdpi.com/2072-4292/10/10/1663.

Hu, J., Liu, L., Yu, H., Guan, L., Liu, X., 2021. Upscaling GOME-2 SIF from clear-sky instantaneous observations to all-sky sums leading to an improved SIF–GPP correlation. Agricult. Forest Meteorol. 306, 108439. http://dx.doi.org/10.1016/j.agrformet.2021.108439, URL https://linkinghub.elsevier.com/retrieve/pii/S0168192321001222.

Joiner, J., Yoshida, Y., Köehler, P., Campbell, P., Frankenberg, C., van der Tol, C., Yang, P., Parazoo, N., Guanter, L., Sun, Y., 2020. Systematic Orbital Geometry-Dependent Variations in Satellite Solar-Induced Fluorescence (SIF) Retrievals. Remote Sens. 12 (15), 2346. http://dx.doi.org/10.3390/rs12152346, URL https://www.mdpi.com/2072-4292/12/15/2346.

Klein, S.A., 1977. Calculation of monthly average insolation on tilted surfaces. Sol. Energy 19 (4), 325–329. http://dx.doi.org/10.1016/0038-092X(77)90001-9, URL https://linkinghub.elsevier.com/retrieve/pii/0038092X77900019.

Köhler, P., Frankenberg, C., Magney, T.S., Guanter, L., Joiner, J., Landgraf, J., 2018. Global Retrievals of Solar-Induced Chlorophyll Fluorescence With TROPOMI: First Results and Intersensor Comparison to OCO-2. Geophys. Res. Lett. 45 (19), 10,456–10,463. http://dx.doi.org/10.1029/2018GL079031, URL https://onlinelibrary.wiley.com/doi/abs/10.1029/2018GL079031.

Kutiel, P., 1992. Slope Aspect Effect on Soil and Vegetation in a Mediterranean Ecosystem. Israel J. Botany 41 (4–6), 243–250. http://dx.doi.org/10.1080/0021213X.1992.10677231, URL https://www.tandfonline.com/doi/abs/10.1080/0021213X.1992.10677231.

Lin, C., Gentine, P., Frankenberg, C., Zhou, S., Kennedy, D., Li, X., 2019. Evaluation and mechanism exploration of the diurnal hysteresis of ecosystem fluxes. Agricult. Forest Meteorol. 278, 107642. http://dx.doi.org/10.1016/j.agrformet.2019.107642, URL https://linkinghub.elsevier.com/retrieve/pii/S0168192319302503.

Lu, X., Liu, Z., Zhao, F., Tang, J., 2020. Comparison of total emitted solar-induced chlorophyll fluorescence (SIF) and top-of-canopy (TOC) SIF in estimating photosynthesis. Remote Sens. Environ. 251, 112083. http://dx.doi.org/10.1016/j.rse.2020.112083, URL https://linkinghub.elsevier.com/retrieve/pii/S0034425720304569.

Magney, T.S., Barnes, M.L., Yang, X., 2020. On the Covariation of Chlorophyll Fluorescence and Photosynthesis Across Scales. Geophys. Res. Lett. 47 (23), http://dx.doi.org/10.1029/2020GL091098, URL https://onlinelibrary.wiley.com/doi/10.1029/2020GL091098.

Mohammed, G.H., Colombo, R., Middleton, E.M., Rascher, U., van der Tol, C., Nedbal, L., Goulas, Y., Pérez-Priego, O., Damm, A., Meroni, M., Joiner, J., Cogliati, S., Verhoef, W., Malenovský, Z., Gastellu-Etchegorry, J.-P., Miller, J.R., Guanter, L., Moreno, J., Moya, I., Berry, J.A., Frankenberg, C., Zarco-Tejada, P.J., 2019. Remote sensing of solar-induced chlorophyll fluorescence (SIF) in vegetation: 50 years of progress. Remote Sens. Environ. 231, 111177. http://dx.doi.org/10.1016/j.rse.2019.04.030, URL https://linkinghub.elsevier.com/retrieve/pii/S0034425719301816.

Morton, D.C., Nagol, J., Carabajal, C.C., Rosette, J., Palace, M., Cook, B.D., Vermote, E.F., Harding, D.J., North, P.R.J., 2014. Amazon forests maintain consistent canopy structure and greenness during the dry season. Nature 506 (7487), 221–224. http://dx.doi.org/10.1038/nature13006, URL http://www.nature.com/articles/nature13006.

Muñoz-Sabater, J., Dutra, E., Agustí-Panareda, A., Albergel, C., Arduini, G., Balsamo, G., Boussetta, S., Choulga, M., Harrigan, S., Hersbach, H., Martens, B., Miralles, D.G., Piles, M., Rodríguez-Fernández, N.J., Zsoter, E., Buontempo, C., Thépaut, J.N., 2021. ERA5-Land: a state-of-the-art global reanalysis dataset for land applications. Earth Syst. Sci. Data 13, 4349–4383. http://dx.doi.org/10.5194/essd-13-4349-2021, https://essd.copernicus.org/articles/13/4349/2021/.

NASA JPL, 2013. NASA Shuttle Radar Topography Mission Global 1 arc second. NASA EOSDIS Land Processes DAAC, http://dx.doi.org/10.5067/MEASURES/SRTM/SRTMGL1.003, URL https://lpdaac.usgs.gov/products/srtmgl1v003/ type: dataset.

Porcar-Castell, A., Tyystjärvi, E., Atherton, J., van der Tol, C., Flexas, J., Pfündel, E.E., Moreno, J., Frankenberg, C., Berry, J.A., 2014. Linking chlorophyll a fluorescence to photosynthesis for remote sensing applications: mechanisms and challenges. J. Exp. Bot. 65 (15), 4065–4095. http://dx.doi.org/10.1093/jxb/eru191.

Richardson, A.D., Keenan, T.F., Migliavacca, M., Ryu, Y., Sonnentag, O., Toomey, M., 2013. Climate change, phenology, and phenological control of vegetation feedbacks to the climate system. Agricult. Forest Meteorol. 169, 156–173. http://dx.doi.org/10.1016/j.agrformet.2012.09.012, URL https://linkinghub.elsevier.com/retrieve/pii/S0168192312002869.

Saleska, S.R., Didan, K., Huete, A.R., da Rocha, H.R., 2007. Amazon Forests Green-Up During 2005 Drought. Science 318 (5850), 612. http://dx.doi.org/10.1126/science.1146663, URL https://www.science.org/doi/10.1126/science.1146663.

Saleska, S.R., Wu, J., Guan, K., Araujo, A.C., Huete, A., Nobre, A.D., Restrepo-Coupe, N., 2016. Dry-season greening of Amazon forests. Nature 531 (7594), E4–E5. http://dx.doi.org/10.1038/nature16457, URL https://www.nature.com/articles/nature16457.

Samanta, A., Ganguly, S., Hashimoto, H., Devadiga, S., Vermote, E., Knyazikhin, Y., Nemani, R.R., Myneni, R.B., 2010. Amazon forests did not green-up during the 2005 drought: AMAZON DROUGHT SENSITIVITY. Geophys. Res. Lett. 37 (5), n/a–n/a. http://dx.doi.org/10.1029/2009GL042154, URL http://doi.wiley.com/10.1029/2009GL042154.

Silleos, N.G., Alexandridis, T.K., Gitas, I.Z., Perakis, K., 2006. Vegetation Indices: Advances Made in Biomass Estimation and Vegetation Monitoring in the Last 30 Years. Geocarto Int. 21 (4), 21–28. http://dx.doi.org/10.1080/10106040608542399, URL http://www.tandfonline.com/doi/abs/10.1080/10106040608542399.

Soenen, S.A., Peddle, D.R., Coburn, C.A., 2005. SCS+C: a modified Sun-canopy-sensor topographic correction in forested terrain. IEEE Trans. Geosci. Remote Sens. 43 (9), 2148–2159. http://dx.doi.org/10.1109/TGRS.2005.852480, URL http://ieeexplore.ieee.org/document/1499030/.

Sun, Y., Frankenberg, C., Jung, M., Joiner, J., Guanter, L., Köhler, P., Magney, T., 2018. Overview of Solar-Induced chlorophyll Fluorescence (SIF) from the Orbiting Carbon Observatory-2: Retrieval, cross-mission comparison, and global monitoring for GPP. Remote Sens. Environ. 209, 808–823. http://dx.doi.org/10.1016/j.rse.2018.02.016, URL https://linkinghub.elsevier.com/retrieve/pii/S0034425718300221.

Teillet, P.M., Guindon, B., Goodenough, D.G., 1982. On the Slope-Aspect Correction of Multispectral Scanner Data. Can. J. Remote Sens. 8 (2), 84–106. http://dx.doi.org/10.1080/07038992.1982.10855028, URL http://www.tandfonline.com/doi/abs/10.1080/07038992.1982.10855028.

Turner, A.J., Köhler, P., Magney, T.S., Frankenberg, C., Fung, I., Cohen, R.C., 2020. A double peak in the seasonality of California's photosynthesis as observed from space. Biogeosciences 17 (2), 405–422. http://dx.doi.org/10.5194/bg-17-405-2020, URL https://bg.copernicus.org/articles/17/405/2020/.

Urraca, R., Huld, T., Gracia-Amillo, A., Martinez-de Pison, F.J., Kaspar, F., Sanz-Garcia, A., 2018. Evaluation of global horizontal irradiance estimates from ERA5 and COSMO-REA6 reanalyses using ground and satellite-based data. Sol. Energy 164, 339–354. http://dx.doi.org/10.1016/j.solener.2018.02.059, URL https://linkinghub.elsevier.com/retrieve/pii/S0038092X18301920.

van der Tol, C., Dolman, A.J., Waterloo, M.J., Raspor, K., 2007. Topography induced spatial variations in diurnal cycles of assimilation and latent heat of Mediterranean forest. Biogeosciences 4 (1), 137–154. http://dx.doi.org/10.5194/bg-4-137-2007, URL https://bg.copernicus.org/articles/4/137/2007/.

Xiao, X., Braswell, B., Zhang, Q., Boles, S., Frolking, S., Moore, B., 2003. Sensitivity of vegetation indices to atmospheric aerosols: continental-scale observations in Northern Asia. Remote Sens. Environ. 84 (3), 385–392. http://dx.doi.org/10.1016/S0034-4257(02)00129-3, URL https://linkinghub.elsevier.com/retrieve/pii/S0034425702001293.

Yang, D., Bright, J.M., 2020. Worldwide validation of 8 satellite-derived and reanalysis solar radiation products: A preliminary evaluation and overall metrics for hourly data over 27 years. Sol. Energy 210, 3–19. http://dx.doi.org/10.1016/j.solener.2020.04.016, URL https://linkinghub.elsevier.com/retrieve/pii/S0038092X20303893.

Zhang, Y., Joiner, J., Alemohammad, S.H., Zhou, S., Gentine, P., 2018a. A global spatially contiguous solar-induced fluorescence (CSIF) dataset using neural networks. Biogeosciences 15 (19), 5779–5800. http://dx.doi.org/10.5194/bg-15-5779-2018, URL https://bg.copernicus.org/articles/15/5779/2018/.

Zhang, Y., Xiao, X., Zhang, Y., Wolf, S., Zhou, S., Joiner, J., Guanter, L., Verma, M., Sun, Y., Yang, X., Paul-Limoges, E., Gough, C.M., Wohlfahrt, G., Gioli, B., van der Tol, C., Yann, N., Lund, M., de Grandcourt, A., 2018b. On the relationship between sub-daily instantaneous and daily total gross primary production: Implications for interpreting satellite-based SIF retrievals. Remote Sens. Environ. 205, 276–289. http://dx.doi.org/10.1016/j.rse.2017.12.009, URL https://linkinghub.elsevier.com/retrieve/pii/S0034425717305801.

Zhang, Z., Zhang, Y., Zhang, Y., Chen, J.M., 2020. Correcting Clear-Sky Bias in Gross Primary Production Modeling From Satellite Solar-Induced Chlorophyll Fluorescence Data. J. Geophys. Res. Biogeosci. 125 (9), http://dx.doi.org/10.1029/2020JG005822.

Zuromski, L.M., Bowling, D.R., Köhler, P., Frankenberg, C., Goulden, M.L., Blanken, P.D., Lin, J.C., 2018. Solar-Induced Fluorescence Detects Interannual Variation in Gross Primary Production of Coniferous Forests in the Western United States. Geophys. Res. Lett. 45 (14), 7184–7193. http://dx.doi.org/10.1029/2018GL077906, URL https://onlinelibrary.wiley.com/doi/abs/10.1029/2018GL077906.